AIAA Aviation
16-20 June 2014, Atlanta, GA
44th AIAA Fluid Dynamics Conference

Measuring Transition and Instabilities in a Mach 6 Hypersonic Quiet Wind Tunnel

Brandon C. Chynoweth*, Christopher A. C. Ward*, Roger T. Greenwood†,
Gregory R. McKiernan*, Roy A. Fisher*, and Steven P. Schneider‡
School of Aeronautics and Astronautics
Purdue University
West Lafayette, IN 47907-1282
Updated: 10 June 2014

This paper presents results for four projects in the Boeing/AFOSR Mach 6 Quiet Tunnel (BAM6QT) at Purdue University. The first project uses an array of discrete roughness elements to interact with second-mode waves on a flared cone. A Rod Insertion Method (RIM) roughness was developed and successfully tested. Controlled nonlinear breakdown of the second-mode waves was observed using temperature sensitive paint and PCB pressure sensors. On a cone at angle of attack, it was found that small roughness near the nosetip had a significant effect on the generation of the stationary vortices. Travelling crossflow waves were measured under both noisy and quiet conditions. The wave properties agreed well with computations by Texas A&M and experiments by TU Braunschweig under similar conditions. The wave amplitudes were reduced significantly when the BAM6QT was run quiet. A high-frequency instability was measured near the breakdown of the stationary waves and disappeared when the sensors were rotated by small angles. This instability may correspond to the secondary instability of the stationary crossflow. Two dimensional roughness was added to a flared cone with a 1-mm radius blunt nosetip. Using the roughness strips, second-mode waves were successfully damped. Finally, measurements made over a cone-ogive-cylinder with interchangeable nosetips show a smooth variation in the entropy-layer instability location as the nosetip angle was increased. Cross-correlations of these measurements provide a better understanding of the entropy-layer instability.

Nomenclature

f	frequency	t	time
M	Mach number	τ	time delay
P	pressure	Θ	phase difference
ϕ	azimuthal angle	x	model axial coordinate
$\dot{q}$	heat flux	y	model spanwise coordinate
Re	Reynolds number		
T	Temperature		

*Research Assistant. Student Member, AIAA
†Research Assistant. Senior Member, AIAA
‡Professor. Associate Fellow, AIAA

Subscripts

0	stagnation condition
wall	wall condition

Abbreviations

BAM6QT	Boeing/AFOSR Mach-6 Quiet Tunnel
TSP	Temperature-Sensitive Paint
PSD	Power-Spectral Density

I. Introduction

A. Hypersonic Laminar-Turbulent Transition

Boundary-layer transition at hypersonic speeds is a process that is difficult to predict. Hypersonic laminar-turbulent transition affects heat transfer, skin friction, separation, and other boundary-layer properties. Therefore, it is important that accurate methods of prediction and control of transition be developed to ensure that flight vehicles are not over-designed. If a hypersonic vehicle is designed to withstand a worst-case scenario, it may have excessive heat shielding. The additional weight of heavy shielding materials would cause the vehicle to suffer from reduced maneuverability and range.

Conventional hypersonic tunnels have noise levels between 1-4%. These noise levels can be more than an order of magnitude larger than noise levels at actual flight conditions and will cause transition to occur earlier than in quiet flow. Quiet wind tunnels are designed to have freestream noise levels that are significantly lower than conventional tunnel. With freestream noise levels of 0.1% or less, quiet wind tunnels provide test conditions that can be used to study laminar-turbulent transition at noise levels similar to flight.

B. The Boeing/AFOSR Mach-6 Quiet Tunnel

The Boeing/AFOSR Mach-6 Quiet Tunnel (BAM6QT) is the larger of two hypersonic quiet wind tunnels in the United States. The BAM6QT is a Ludweig tube design incorporating a long driver tube with a converging-diverging nozzle at the downstream end. A schematic of the tunnel is shown in Figure 1. To operate the tunnel, a pair of diaphragms downstream of the test section are burst causing an expansion fan to propagate upstream through the test section and driver tube. The air behind the expansion fan is accelerated through the nozzle to create Mach-6 flow in the test section.

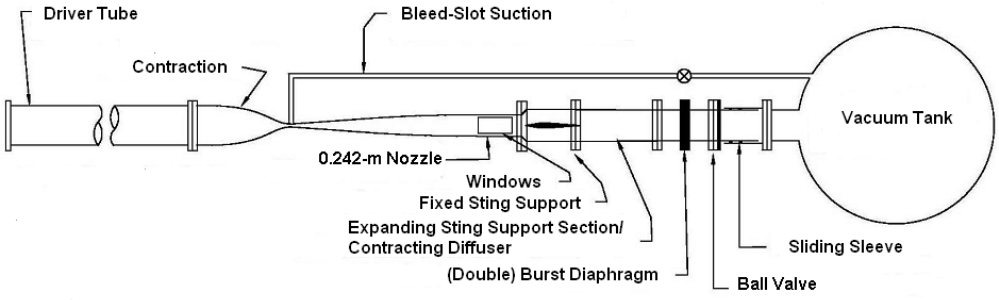

Figure 1. Schematic of Boeing/AFOSR Mach 6 Quiet Tunnel.

Using several unique features, the BAM6QT is able to produce noise levels on the order of 0.05% for stagnation pressures up to 170 psia. A suction slot upstream of the throat is connected to the vacuum tank and can be used to remove the boundary layer on the nozzle wall at the throat. This allows for a fresh laminar boundary layer to grow on the nozzle wall starting near the throat. If the operator chooses not to use the suction slot, the tunnel can be operated with noise levels of the order of 3%, similar to conventional hypersonic facilities. The long divergent portion of the nozzle was designed to minimize the growth of Görtler instabilities and is polished to a mirror finish. Additionally, to reduce the risk of particulate matter

scratching the mirror finish, sub-micron air filters are used to remove particles in the air used to pressurize the driver tube.

II. Transition and Instabilities Measurements on a Flared Cone

A. Brief Background and Previous Experiments

The flared cone was designed to study the non-linear transition process in a hypersonic boundary layer. The shape of the cone maintains a constant thickness boundary layer. Since the frequency of the dominant second mode wave is nearly constant, large amplitude waves can be generated. Using TSP images, the transition process can be observed experimentally. Streaks of increased temperature occur on the cone followed by a decrease to near laminar levels. If the Reynolds number is large enough, a second increase in heating is observed. This second increase in heating is due to the flow transitioning to turbulence, as has been verified using pressure fluctuation measurements.[1]

The goal of the present work is to control the streaks through the use of discrete roughness elements. Chou first used nail polish dots to alter the second-mode waves. Her results showed that discrete roughness elements could affect the streaks, but the nail polish proved difficult to apply in a consistent manner.[2] Luersen tested several methods including rub-on dots, metallic wafer inserts, and epoxy dots applied with an electronic fluid dispensing device. The epoxy dots could be applied in a consistent manner. The epoxy dots that Luersen produced were either too small to have an effect on the streaks, or they were too large and caused the flow to transition without interacting with the second-mode waves.[1,3] An epoxy dot with a height of 305 μm was then tested on the 4-inch-base flared cone and was found to interact with the second mode waves rather than act as a boundary layer trip.[4] Further testing with the epoxy could not be performed efficiently because the favorable properties of the epoxy could not be duplicated with newer batches due to an aging effect. Therefore, the present research focuses on the development and testing of a new method of creating an array of discrete controlled roughness elements.

B. Development of New Roughness Inserts Using a Rod Insertion Method (RIM)

The 5-inch base flared cone was manufactured with a removable ring 25.5 cm from the nosetip. The ring can be used to test destructive and non-destructive roughness creation methods. A new method was developed where brass rods are inserted perpendicular to the surface of the insert and then machined down to the proper height. This rod insertion method will be referred to as the RIM roughness. A picture of the resulting insert is shown in Figure 2. Using this method, each insert takes only 3 to 4 hours to manufacture. Additionally, the height, diameter, and spacing between roughness elements can be controlled and varied to see the effects of each independent variable. The RIM roughness was first tested with a 5-inch base diameter flared cone, but tunnel starting issues made it impossible to test at stagnation pressures less than 170 psia. As a result, a 4.5-inch base diameter cone with the same 3 meter flare was made. Tests with the smaller diameter were successful at stagnation pressures from 100 psia up to the maximum BAM6QT quiet pressure of 170 psia.

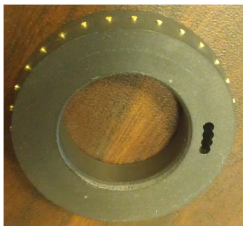

Figure 2. RIM roughness with brass rods of height = 381 μm and diameter = 838 μm.

C. Results without Roughness Present

In order to compare the effects of different roughness elements, it is necessary to have a baseline for the TSP images and the power spectral density (PSD) data from the PCB pressure sensors for the nominally smooth cone, when no controlled roughness is present. Figures 3(a) and 3(c) show the TSP results at unit Reynolds numbers of 7.7×10^6/m and 9.2×10^6/m, respectively. By counting the number of streaks between the spanwise registration marks which are separated by 30°, the circumferential wave number is calculated to be approximately 96. In Figure 3(a) the initial increase in heating can be seen approximately 47 cm from the nosetip. With an increase in unit Reynolds number, the initial increase in heating moves upstream by 5 cm.

Figure 3(b) and Figure 3(d) show the PSD for the corresponding Reynolds numbers of 7.7×10^6/m and 9.2×10^6/m, respectively. In Figure 3(b) second mode waves centered around a frequency of 270 kHz are measured. Harmonics of this main frequency are observed at 540 kHz and 810 kHz. A new feature that has not been measured in the past is the peak near 940 kHz for the three PCB sensors farthest downstream. In Figure 3(d), at an increased unit Reynolds number, the second mode waves are centered around 295 kHz. As the Reynolds number increases, the boundary layer thins, and a higher second-mode wave frequency is expected. At the farthest downstream location, an increase in broadband noise can be seen indicating that transition to turbulence has started.

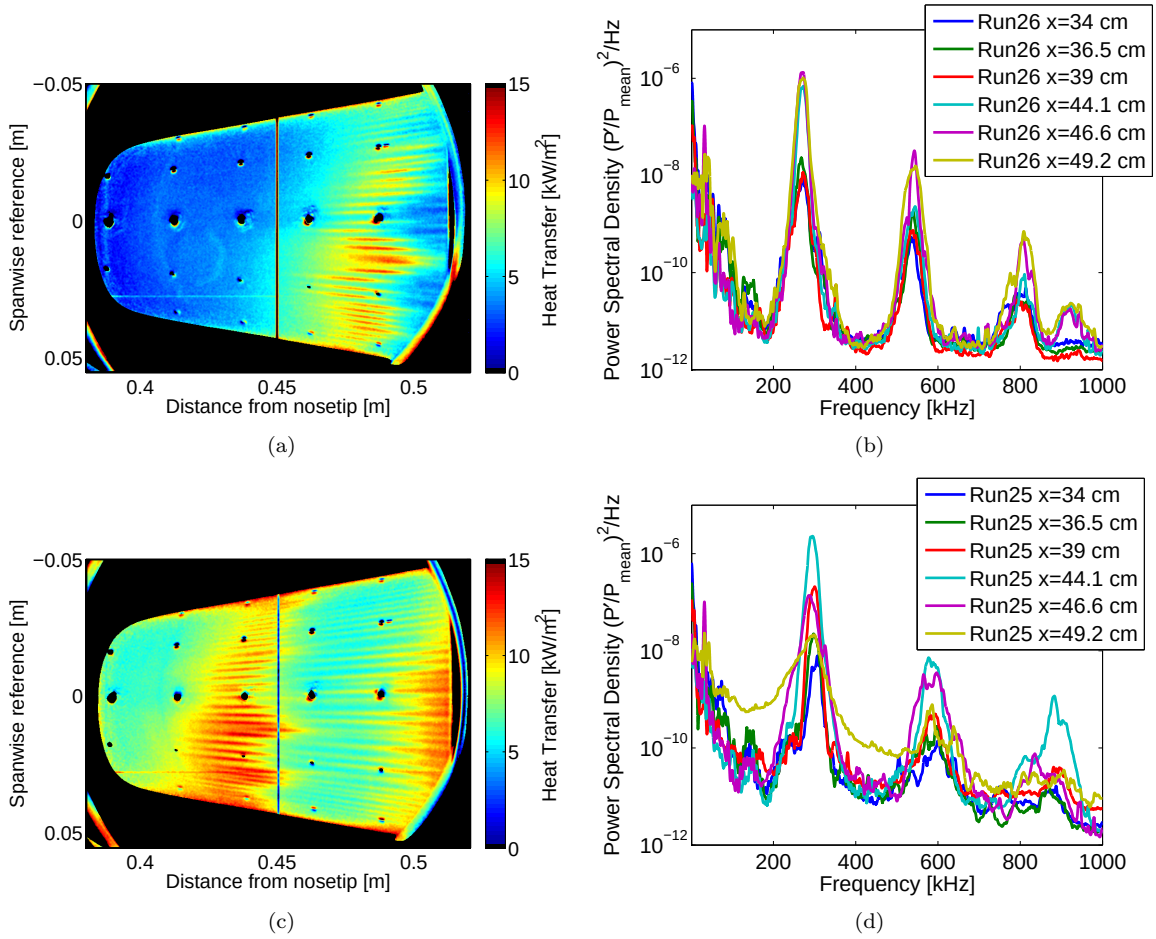

Figure 3. TSP images and the corresponding power spectral densities without roughness elements at (a,b) Re = 7.7×10^6/m, P_0 = 102.6 psia, T_0 = 435 K and (c,d) 9.2×10^6/m, P_0 = 121.4 psia, T_0 = 435 K.

D. Results with RIM Roughness Inserts

The first RIM roughness tested used 30 equally spaced brass rods with diameters of 838 μm. The rods extended 381 μm above the cone surface. At a unit Reynolds number of 7.8×10^6/m, a new pattern of streaks is observed, as shown in Figure 4(a). At 45.0 cm downstream of the tip of the model, two sets of streaks are observed, offset by approximately 2 cm. Farther downstream, pairs of streaks are observed. Each streak pair is directly downstream from a single roughness element. The PSD shows that the second mode wave is still centered at 270 kHz, but the harmonics at 540 kHz and 810 kHz have been damped when compared to the model without any roughness. At a higher Reynolds number, Figure 4(c), the streak pairs from the roughness elements dominate the TSP image. The PCB pressure sensor at x = 46.6 cm shows an increase in broadband noise indicating transition, and by x = 49.2 cm the pressure sensor indicates the boundary layer is turbulent. While turbulence does occur farther upstream than in the nominal no-roughness case, these roughness elements do not appear to act as boundary layer trips.

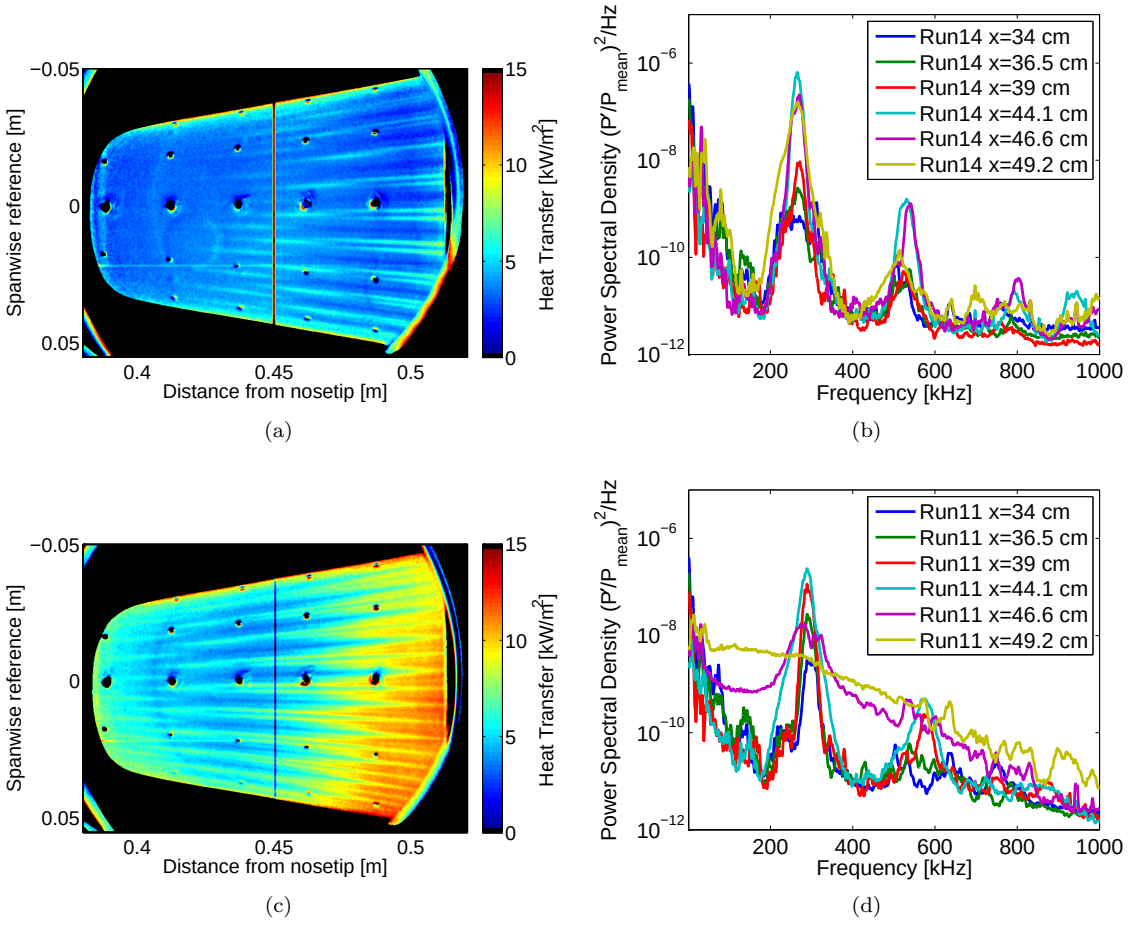

Figure 4. TSP images and the corresponding power spectral densities with roughness elements of diameter = 838μm and height = 381μm at (a,b) Re = 7.8×10^6/m, P_0 = 102.9 psia, T_0 = 433 K and (c,d) 9.4×10^6/m, P_0 = 121.8 psia, T_0 = 429 K.

The next RIM roughness that was tested again used 30 equally spaced brass rods with a diameter of 838 μm, but the height was decreased to 254 μm above the cone surface. At a unit Reynolds number of 7.9×10^6/m, the complexity of the streak pattern is apparent in Figure 5(a). Using the PCB pressure sensors, second-mode waves at 270 kHz and harmonics at 540 kHz and 810 kHz were measured. There is an additional peak at 940 kHz that is first measured 44.1 cm from the nosetip; proceeding downstream it decreases in amplitude. The cause of this peak has not been determined. The presence of second-mode waves but with a different TSP streak pattern indicates that the 254 μm roughness is interacting with the second mode waves, rather than acting as a boundary layer trip.

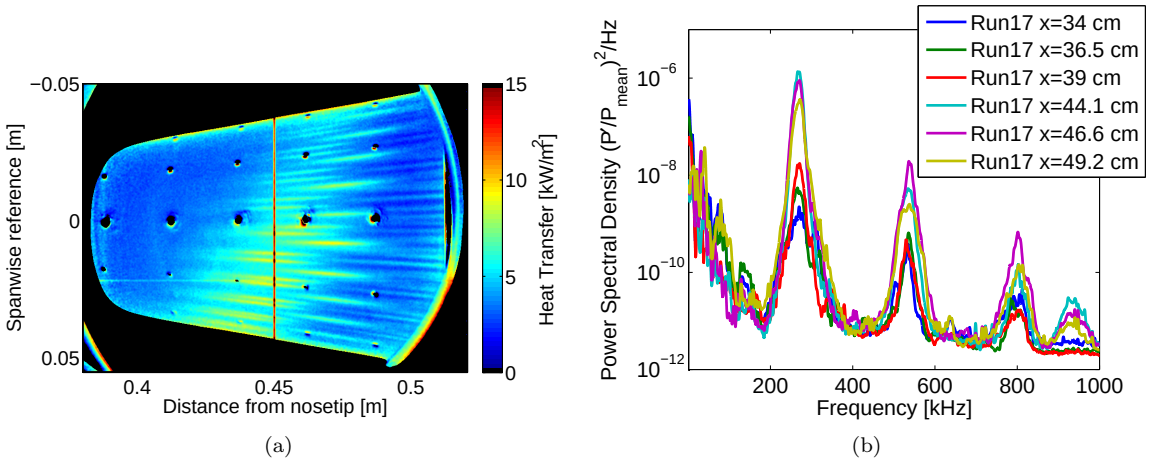

Figure 5. (a) TSP image and (b) PCB power spectral density with roughness elements of diameter = 838μm and height = 254μm at Re = 7.9×10^6/m, P_0 = 103.4 psia, T_0 = 432 K.

In order to better quantify the streak pattern, three azimuthal traces of the surface heating were analyzed. Figure 6(a) and Figure 6(b) compare these azimuthal cuts. When comparing azimuthal cuts, the heat transfer has been normalized by the maximum value in order to make quantitative comparisons easier. Figure 6(c) shows a TSP image where the exact location of the azimuthal traces are marked. When moving downstream, the first increase in heating is due to the streak pairs formed directly downstream of the roughness elements as shown in Figure 6(a) at x = 45.4 cm. Continuing downstream, a single streak forms directly between the streak pairs. Finally, at a spanwise cut location of x = 48.7 cm, the streak pairs are no longer present, but in their place single faint streaks spaced 12° apart can be observed as shown in Figure 6(b).

At an increased unit Reynolds number of 9.2×10^6/m, the characteristic hot-cold-hot phenomenon is observed, as shown in Figure 7(a), but the streak pattern is decidedly different than when no roughness elements are present. The hot-cold-hot phenomena has been simulated by Sivasubramanian and Fasel.[5] The initial increase in heating is due to the large amplitude and saturation of the primary wave. As the primary wave decays following nonlinear saturation, the heating decreases creating the colder region. Finally, as the higher modes start to experience nonlinear saturation the heating increases again. The roughness elements introduce perturbations that interact with the second-mode waves. Additional DNS computations with roughness elements present would further the understanding of the this interaction and the nonlinear breakdown process. Figure 7(b) shows that second mode waves are present, but the beginning of transition is measured with a PCB pressure sensor 46.6 cm from the nosetip versus 49.2 cm from the nosetip when no roughness is present.

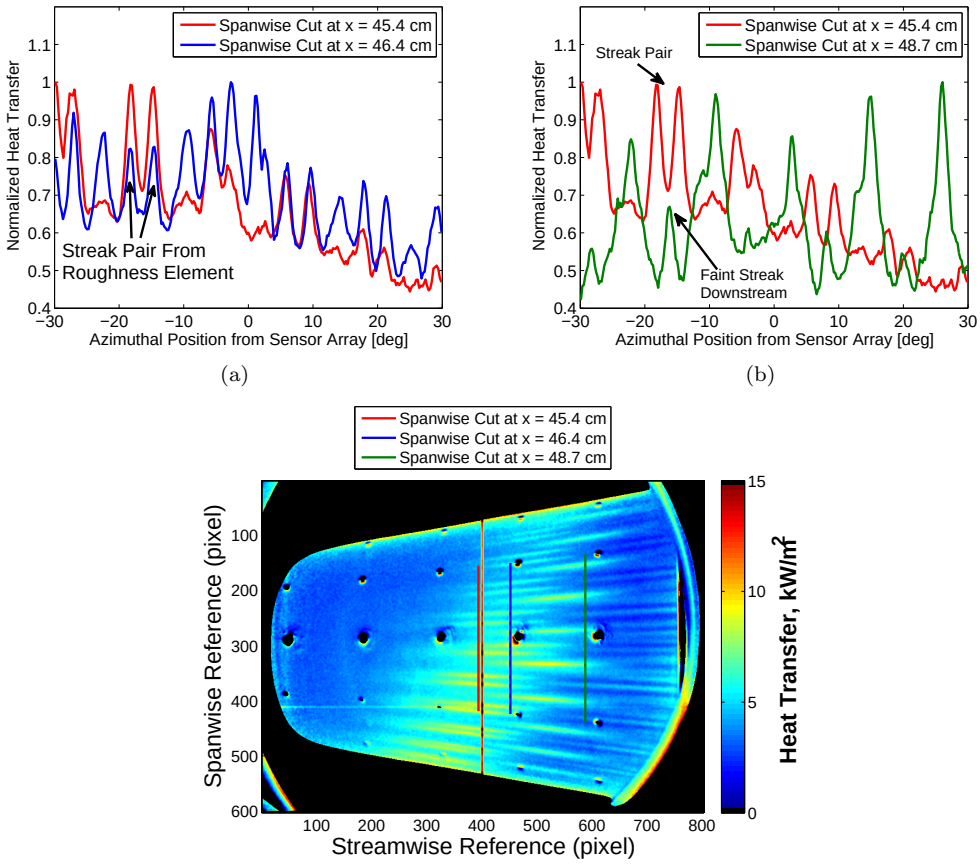

Figure 6. (a),(b) Azimuthal cuts for comparison of streak patterns with a TSP image (c) showing location of azimuthal cuts. Roughness element diameter = 838 μm and height = 254 μm at at Re = 7.9$\times 10^6$/m, P_0 = 103.4 psia, T_0 = 432 K.

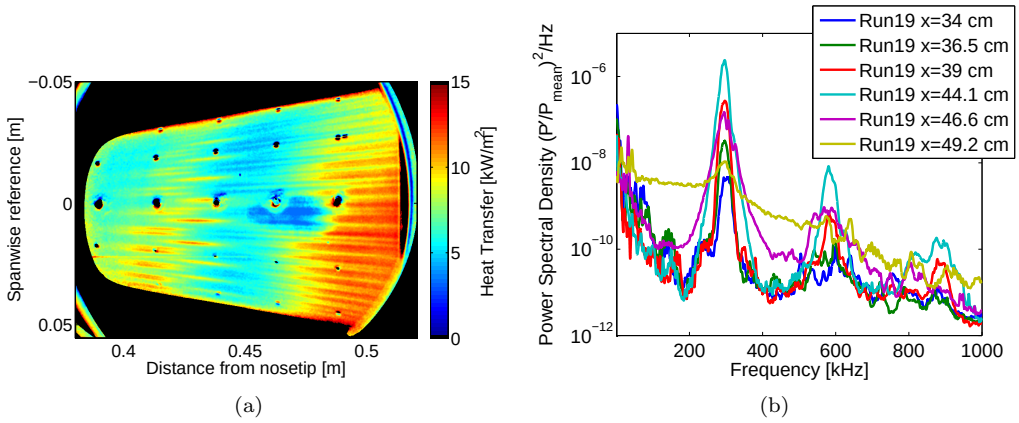

Figure 7. (a) TSP image and (b) PCB power spectral density with roughness elements of diameter = 838μm and height = 254μm at 9.2$\times 10^6$/m, P_0 = 121.4 psia, T_0 = 435 K.

III. Crossflow Instability and Transition on a Cone at Angle of Attack

A. Introduction and Background

There are several instabilities that can cause transition in a three-dimensional boundary layer, including the centrifugal, streamwise, and crossflow instabilities. For an axisymmetric cone in hypersonic flow pitched at an angle of attack, a circumferential pressure gradient is created due to a stronger shock near the windward ray. The circumferential pressure gradient causes the inviscid streamlines to be curved. In the boundary layer, there is an imbalance between the pressure gradient and the centripetal acceleration because the streamwise velocity is reduced, but the pressure gradient does not change. This imbalance causes a secondary flow (crossflow) in the boundary layer perpendicular to the inviscid streamlines. Crossflow must vanish at the wall and the edge of the boundary layer, creating an inflection point in the crossflow velocity profile.[6] Crossflow is thus inviscidly unstable and manifests as co-rotating vortices centered around the inflection point. Crossflow waves can be either travelling or stationary with respect to the surface. It has been verified experimentally for low speeds that the stationary waves tend to dominate in low-disturbance environments such as in flight or in low-noise tunnels, while the travelling waves tend to dominate in high-disturbance environments such as conventional tunnels.[7] It is not known if this is the case for hypersonic flows.

The stationary waves appear to be sensitive to small roughness placed near the wave's neutral point. Both Saric (at low speeds) and Corke (at high speeds) have had much success in using discrete roughness elements to control the stationary vortices.[6,8–10] Depending on the spacing of the roughness, certain stationary vortex wavelengths can be forced, and crossflow-induced transition can be delayed.

When the stationary instability becomes saturated, a high-frequency secondary instability appears.[11] The secondary instability travels along the stationary vortex, and appears as a ring-like vortex.[12] The secondary instability is created by an inflectional velocity profile in the high shear layer between the stationary vortex and the edge of the boundary layer. The frequency of the secondary instability at low speeds was found to be approximately an order of magnitude larger than the primary travelling instability.[13] Computations have been performed looking at the secondary instability of the stationary mode at transonic speeds on a swept wing,[14,15] and a method for correlating transition location with secondary-mode N-factors has been studied,[11] but limited work has been done at hypersonic speeds.

All crossflow-instability experiments presented in this section were performed with a 7° half-angle cone at 6° angle of attack. Global heat transfer was obtained from calibrated temperature-sensitive paint data. A more detailed description of the calibration method is given in Reference 1. Pressure measurements were obtained using PCB and Kulite fast-pressure transducers. A drawing of the cone is shown in Figure 8. All the pressure measurements shown are from the two furthest downstream sensor locations (0.32 and 0.36 m from the nosetip). The downstream sensors are offset 30° in the azimuthal direction. The Kulite array consists of four Kulites offset 2.25° in the azimuthal direction, and 1.7 mm in the axial direction.

B. Effect of Controlled Roughness on Stationary Crossflow Waves

The discrete roughness elements, or dimples, were added to the roughness insert section of the cone by pressing a conical stainless steel rod into a Torlon piece, shown in Figure 9. This method is similar to the one used by Schuele.[16] Fifty evenly spaced discrete roughness elements were placed around the azimuth, 50.8 mm (2 inches) axially from the nosetip, near the neutral point of most amplified stationary waves based on computations by Li et al.[17]

A Mitutoyo Surftest SJ-301 surface roughness profilometer was used to measure the profile of the dimples, shown in Figure 10. A smooth case was added for reference. When the stainless-steel rod was pressed into the Torlon, some material was pushed out, creating the peaks seen in the profile. Therefore, the effective depth and diameter of the dimple is approximately 70 μm and 600 μm respectively (based on where the profile departs and returns to the smooth case). There is some uncertainty in the measurements since it is not known if the profilometer traversed the middle of the dimple, and therefore the depth and diameter may be inaccurate. It is difficult to determine the uniformity of the dimples used in the experiments due to the errors associated with the measuring technique. More advanced measuring techniques are being explored.

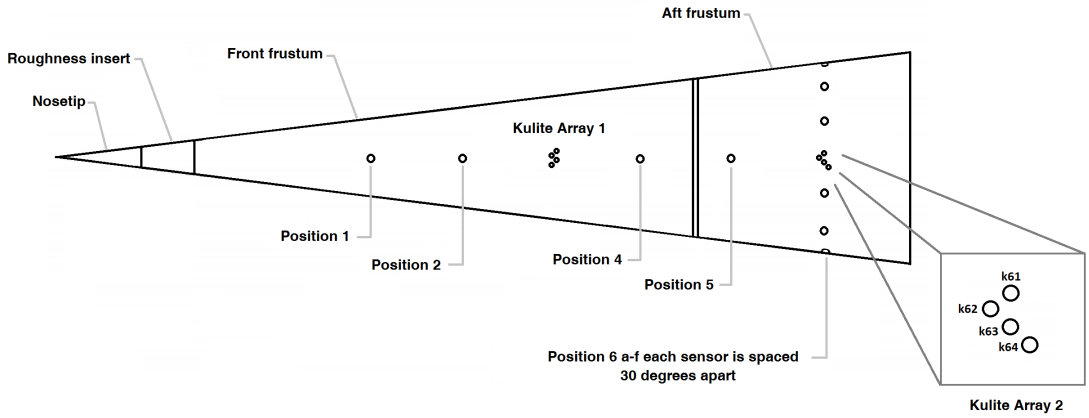

Figure 8. 0.4 m long 7° half angle cone with sensor locations.

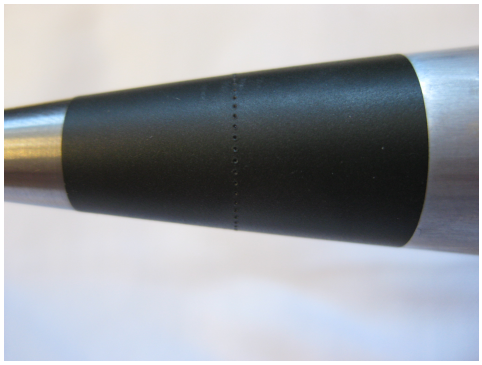

Figure 9. Torlon section and 50 roughness-elements (dimples).

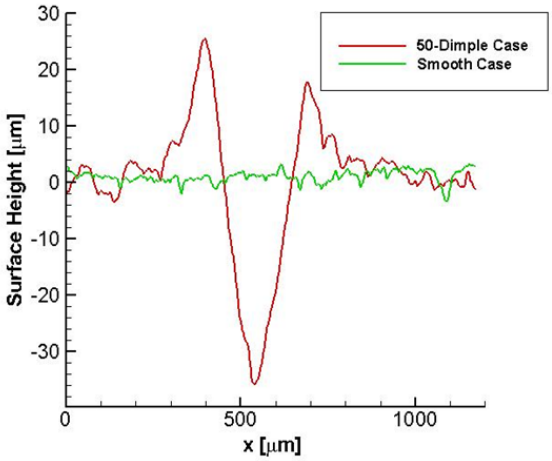

Figure 10. Profile of discrete roughness element (dimple).

Data with the 50-dimpled and smooth Torlon inserts are shown in Figure 11. Two different Reynolds numbers were tested under quiet flow, and the lee side of the cone was imaged. The images on the right side are smooth, and the images on the left are with the 50 dimples. At the lower Reynolds number, the roughness elements produce larger amplitude stationary vortices. The effect of the roughness elements become more pronounced at the higher Reynolds number. When the roughness is added, a much different pattern of stationary vortices is created and transition appears to be delayed compared to the smooth case. It is not known why the roughness elements produce larger-amplitude stationary vortices at the lower Reynolds number but smaller-amplitude stationary vortices at the higher Reynolds number (as compared to the smooth cases). At the larger Reynolds number, the roughness elements appear to be creating a more regular pattern of stationary vortices compared to the smooth case, and therefore appear to be dominating the generation of the stationary vortices. For the nominally smooth case, the stationary vortices are thought to arise from the random roughness on the cone.

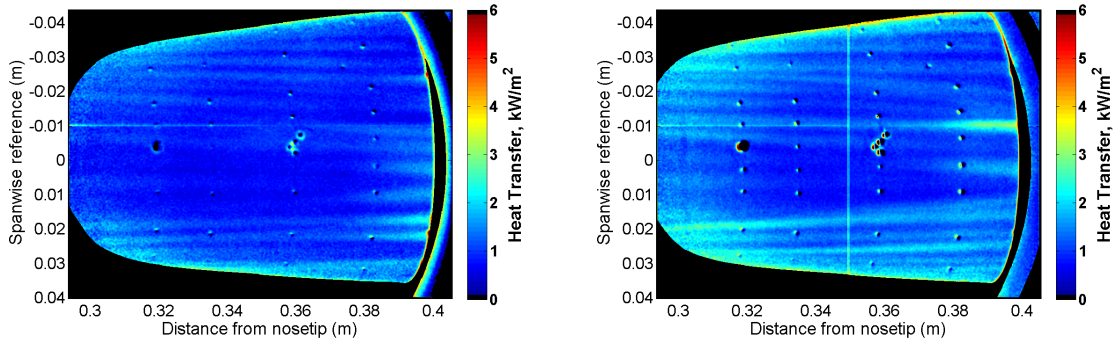

(a) Smooth. Re = 8.2×10^6/m, P_0 = 109 psia, T_0 = 426 K, T_{wall} = 301 K.

(b) Torlon Roughness. Re = 8.1×10^6/m, P_0 = 109 psia, T_0 = 429 K, T_{wall} = 297 K.

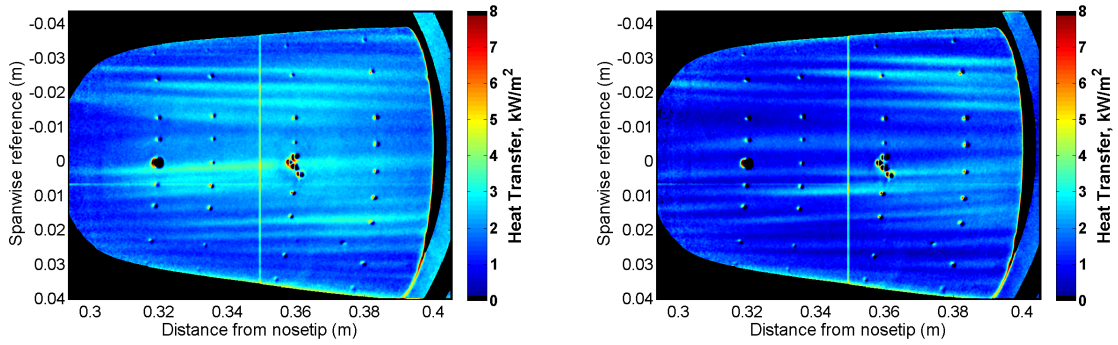

(c) Smooth. Re = 10.5×10^6/m, P_0 = 139 psia, T_0 = 425 K, T_{wall} = 303 K.

(d) Torlon Roughness. Re = 10.4×10^6/m, P_0 = 139 psia, T_0 = 428 K, T_{wall} = 299 K.

Figure 11. TSP images under quiet flow and varying Reynolds number with smooth and rough Torlon inserts (50 dimples). Lee side of the cone imaged.

Spanwise heat transfer profiles of the TSP images in Figure 11 are shown in Figure 12. The spanwise profiles are at an axial location of 0.37 m. The lower Reynolds number case does not show a significant difference in the spanwise profiles, but the stationary vortices differ near 190–220°. Again, the effect of the roughness elements is much clearer at the higher Reynolds number, where the roughness elements generate a more regular pattern of stationary vortices. The approximate wavenumber (between 140 and 220 degrees) for the smooth case is 40 and for the 50 dimple case is 54. The difference in wavenumber between the number of dimples and the measured wavenumber (at an axial distance of 0.37 m) may be due to streamline spreading. Additional data are currently being analyzed with differing roughness depths, heights, diameters, and spacing.

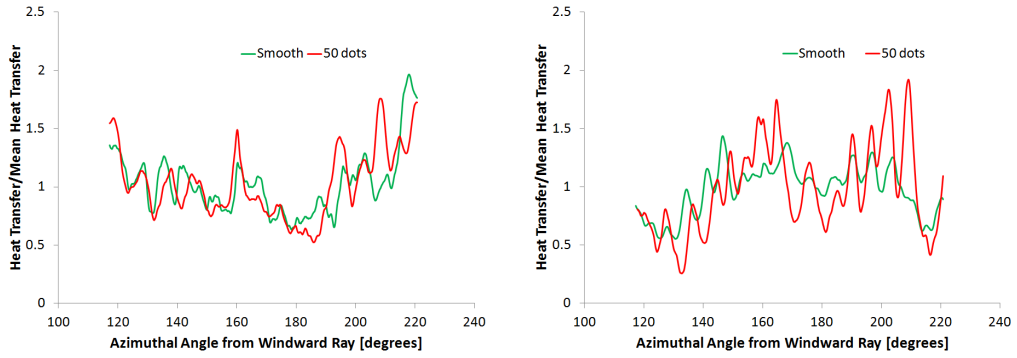

(a) Re - 8.2×10^6/m. (b) Re - 10.5×10^6/m.

Figure 12. Spanwise heat transfer profiles at x = 0.37 m of TSP images in Figure 11.

C. Properties of the Travelling Crossflow Waves

In order to calculate the properties of the travelling crossflow waves, including phase speed and propagation angle, measurements from 3 or 4 sensors are required. The more general case utilizes four sensors, as discussed in Reference 18. The method in References 19 and 20 utilizes three sensors, and is also used by the author. The cross spectrum of two signals $s_1(t)$ and $s_2(t)$ is defined as:

$$S_{12}(f) = \lim_{T\to\infty}(1/T)E[\hat{s_1}^*(f,T)\hat{s_2}(f,T)] \tag{1}$$

where $\hat{s}$ represents the Fourier transform of the signal, * is the complex conjugate and E[] is the expected value operator.

The magnitude-squared coherence (γ^2) determines how well a signal $s_1(t)$ correlates to another signal $s_2(t)$ at each frequency and is defined as:

$$\gamma^2(f) = \frac{|S_{12}(f)|^2}{S_{11}(f)S_{22}(f)} \tag{2}$$

The magnitude-squared coherence yields values between 0 and 1, where 0 represents no correlation and 1 represents a perfect correlation.

The phase difference (Θ) between the two signals is determined by the following equation

$$\Theta(f) = \arctan\left[\frac{\Im(S_{12})}{\Re(S_{12})}\right] \tag{3}$$

and the time delay (τ) between the two signals is determined by

$$\tau(f) = \frac{\Theta(f)}{2\pi f}. \tag{4}$$

A diagram of the Kulite sensor array is shown in Figure 13(a). The x-axis is the axial coordinate on the cone's surface, and the y-axis is the circumferential coordinate in a tangent plane to the cone's surface near the region of the sensors. The coordinate system can then be rotated by an angle Ψ, shown in Figure 13(b). Ψ represents the angle between the wave propagation and the x-axis. For most experiments, sensor 1 was closest to the leeward ray and sensor 4 was closest to the windward ray.

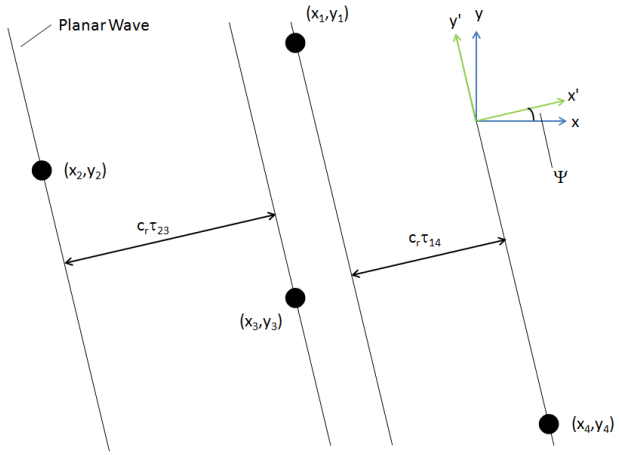

(a) Original Coordinate System with planar wave

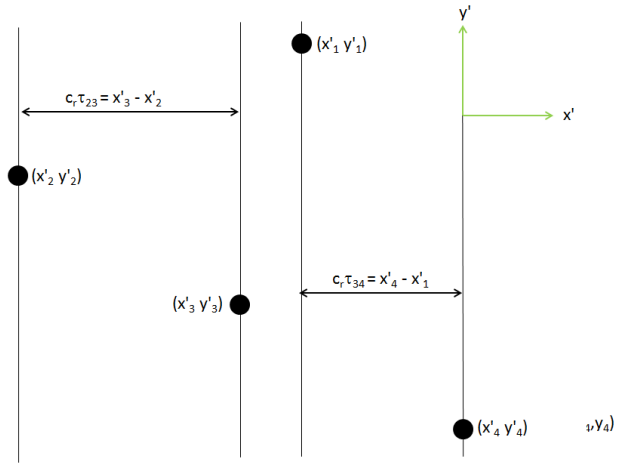

(b) Rotated Coordinate System

Figure 13. Diagram of Kulite sensor array. Not to scale.

Points in the original coordinate system (x,y) can be transformed into the rotated coordinate system (x',y') with the following equations:

$$x' = x\cos\Psi + y\sin\Psi \tag{5}$$

$$y' = -x\sin\Psi + y\cos\Psi \tag{6}$$

The phase speed of the wave (c_r) multiplied by the time delay of a phase surface between two sensors (τ_{12}) is simply the distance between the two sensors in the rotated coordinate system

$$c_r\tau_{12} = x'_2 - x'_1 \tag{7}$$

Plugging in equation 5 into equation 7 yields the following result:

$$c_r \tau_{12} = (x_2 - x_1)\cos\Psi + (y_2 - y_1)\sin\Psi \tag{8}$$

Utilizing equation 8 for two sensor pairs (1,2) and (3,4), the propagation angle and phase speed can be determined:

$$\Psi = \arctan\left[\frac{\tau_{34}(x_2 - x_1) - \tau_{12}(x_4 - x_3)}{\tau_{12}(y_4 - y_3) - \tau_{34}(y_2 - y_1)}\right] \tag{9}$$

$$c_r = \frac{(x_2 - x_1)\cos\Psi + (y_2 - y_1)\sin\Psi}{\tau_{12}} \tag{10}$$

The only restriction for this analysis is that sensor $1 \neq 2$ and sensor $3 \neq 4$. Therefore this analysis can be done with 3 or 4 sensors.

D. Measurements of Travelling Crossflow Wave Properties

Measurements were made with the array of Kulite sensors on the 90° ray under both noisy and quiet flow for Reynolds numbers of 6.5×10^6/m and 11.5×10^6/m, respectively. The PSD of the Kulites is shown in Figure 14. Under both noisy and quiet flow, the PSD shows a low-frequency peak in the spectra near 30–40 kHz. The same low-frequency instability was previously measured, as reported in Reference 4, and the low-frequency instability was assumed to be the travelling crossflow insability. Additional data will be presented here confirming that the low-frequency does correspond to the travelling crossflow instability.

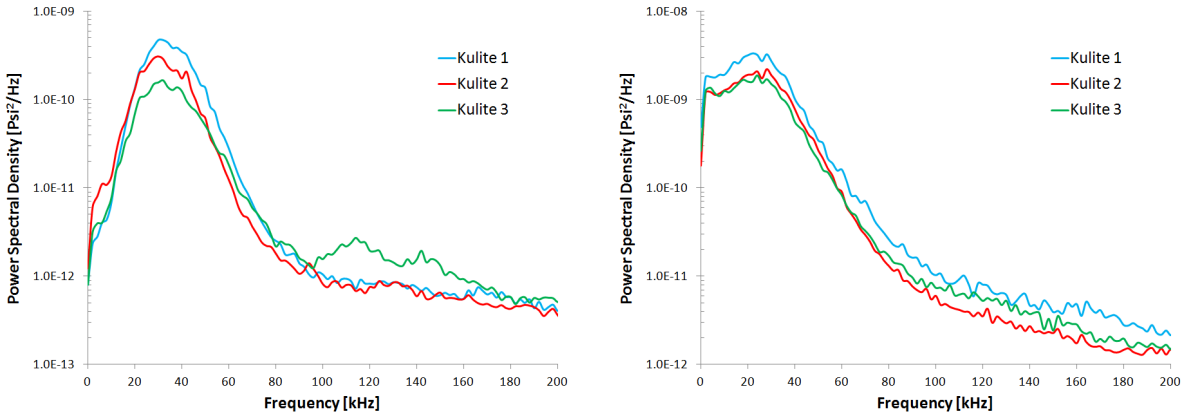

(a) Quiet, Re - 11.5×10^6/m

(b) Noisy, Re - 6.5×10^6/m

Figure 14. PSD of Kulites measuring a low-frequency instability under both noisy and quiet flow. Sensors on the 90° ray (measured from the windward ray).

Utilizing the array of Kulite sensors, the wave angle and phase velocity of the low-frequency instability can be calculated to better determine if the instability is in fact due to the travelling crossflow. Figure 15 shows the PSD, magnitude-squared coherence, phase difference and time delay for the 11.5×10^6/m Reynolds number case under quiet flow. It was decided to only look at frequencies with a magnitude-squared coherence greater than 0.2, based on work by Kimmel et al.[21] Figures 15(c) and 15(d) show that the wave is passing over sensor 1, sensor 2 and sensor 3 in that order.

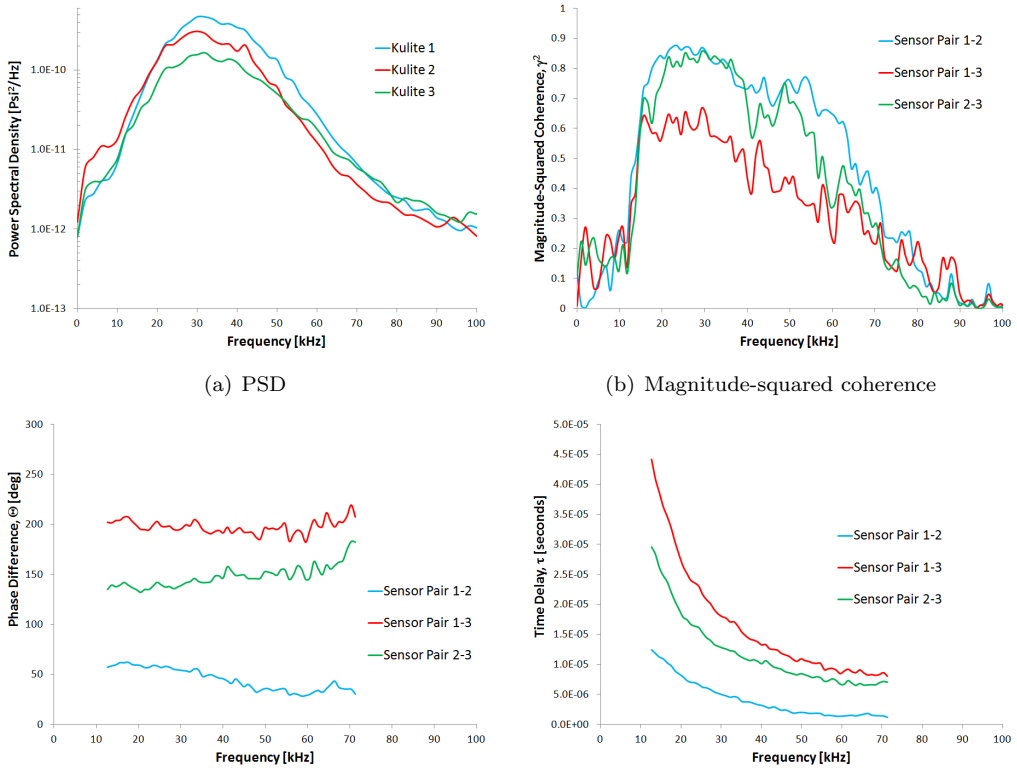

(a) PSD

(b) Magnitude-squared coherence

(c) Phase difference

(d) Time delay

Figure 15. Sample PSD, magnitude-squared coherence, phase difference and time delay for Re - 11.5×10^6/m.

Figure 16 plots the wave angle and phase speed, utilizing equations 9 and 10, for various Reynolds numbers where the low-frequency instability is measured. The wave angle is measured with respect to an axial axis from the nosetip along the cone's surface, where negative angles correspond to waves travelling from the leeward to windward ray (opposite direction of crossflow). Table 1 contains the wave angle and phase speed at the peak frequency for each case. For all cases, whether noisy or quiet, the wave angle is approximately -65°. The fact that the most amplified travelling waves travel in the opposite direction of the crossflow agrees with computations by Malik et al,[22] although the computations were done at low speeds on a swept wing. Comparing the noisy and quiet cases, the peak frequency is lower for the noisy cases. This is likely caused by sevearl reasons. The Mach number is 5.8 when the BAM6QT is run noisy, the Reynolds number is lower for the noisy tests, leading to a thicker boundary layer and therefore lower frequencies, and the differing noise levels may also amplify different frequencies of travelling waves. Despite having different peak frequencies, the wave propagation angle is approximately constant regardless of the noise level. Focusing on the quiet cases, a slight drop in Reynolds number does not cause a change in the propagation angle, but the phase speed is lower. It was not possible to make a direct Reynolds number comparison under noisy and quiet flow. If the noisy Reynolds number was increased the flow over the sensors was turbulent, and if the quiet Reynolds number was decreased the waves were too weak to measure.

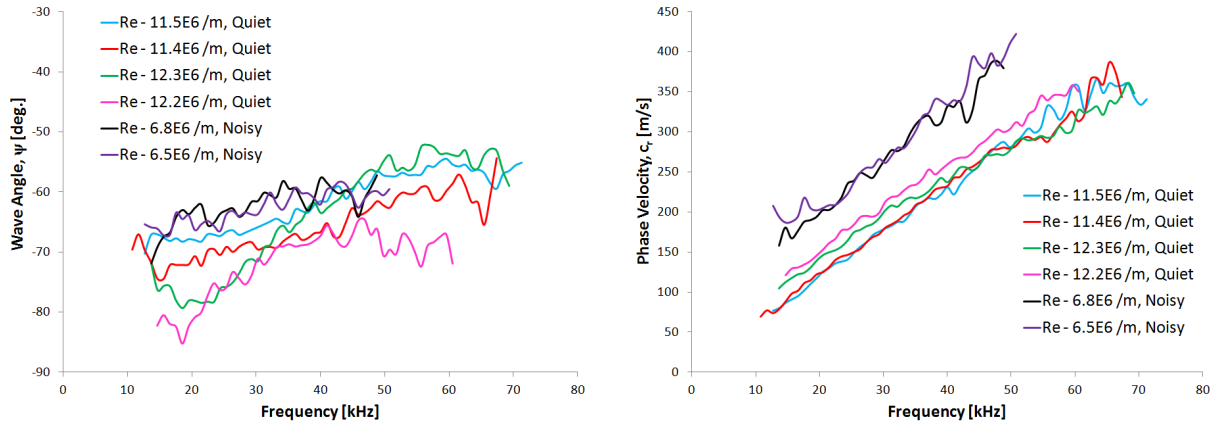

(a) Wave Angle

(b) Phase Speed

Figure 16. Wave angle and phase speed for low-frequency instability wave.

Noise Level	Reynolds Number [/m]	Peak Frequency [kHz]	Wave Angle [degrees]	Phase Speed [m/s]
Quiet	12.3×10^6	32–38	-62 to -68	206–232
Quiet	12.2×10^6	32–40	-67 to -70	220–259
Quiet	11.5×10^6	30–34	-64 to -65	179–197
Quiet	11.4×10^6	28–36	-66 to -68	169–212
Noisy	6.8×10^6	22–26	-62 to -65	208–248
Noisy	6.5×10^6	24–28	-63 to -66	222–255

Table 1. Wave angle and phase speed corresponding to the peak frequency of the low-frequency instability wave at differing conditions.

Munoz performed similar experiments in the Hypersonic Ludwieg Tube Braunschweig (HLB) at TU Braunschweig on a 7° half-angle cone at 6° angle of attack with a nominally sharp nosetip.[23] He measured an instability with a frequency between 35 and 40 kHz and a propagation angle between 62 and 70°. Computations by Perez[24] showed that this low-frequency instability corresponds to the travelling crossflow. Computations by Li et al[17] also show that the travelling crossflow waves with the largest N-factors (between 10 and 20) have a frequency between 20 and 65 kHz. Based on all of this, it appears that the low-frequency instability measured by the author is the travelling crossflow instability.

E. Comparison to TU Braunschweig Measurements

Additional comparisons can be made between the data collected in the TU Braunschweig conventional tunnel (HLB) by Munoz[23] and the data from the quiet tunnel at Purdue. HLB has a free-stream noise level of 1–1.5% and a Mach number of 5.8–5.95. When the BAM6QT is run noisy, the freestream noise level is 3% and the Mach number is 5.8. Under quiet flow, the BAM6QT has a freestream noise level of 0.05% and a Mach number of 6.0.

Figure 17 plots the PSD of pressure measurements from both tunnels under noisy flow. The HLB data were collected from a PCB sensor on the 90° ray, 0.257 m from the nosetip. The BAM6QT data were collected from a PCB sensor 0.321 m from the nosetip and a Kulite sensor 0.362 m from the nosetip, with both sensors on the 90° ray. The Reynolds number is based on the distance from the nosetip along the centerline. Both the HLB and BAM6QT raw datasets were analyzed with the same MATLAB code and non-dimensionalized by the theoretical edge pressure of a 7° cone at 0° AoA.

All the sensors show a low-frequency travelling crossflow instability, near 30 to 40 kHz. The difference in amplitudes between the measurements made in the two tunnels with the PCB sensors is likely caused by slightly differing conditions, tunnel noise levels, and sensor calibrations. The Kulite in the BAM6QT also measures the travelling waves, at a slightly lower frequency (likely because the sensor is further downstream than the PCBs).

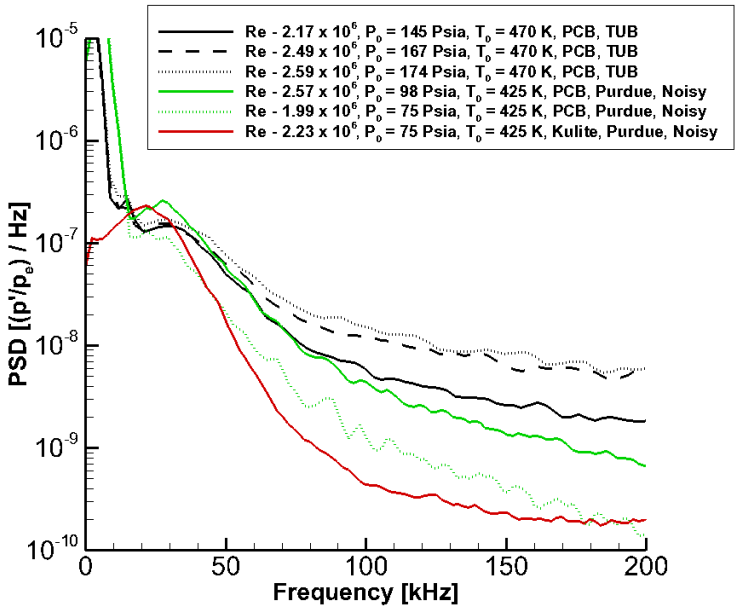

Figure 17. PSD of Kulite and PCB sensors in both the HLB and BAM6QT under noisy flow. HLB PCB at x = 0.257 m from nosetip. BAM6QT PCB at x = 0.321 m and Kulite at x = 0.362 m from the nosetip.

The BAM6QT was also run quiet, and this data is shown along with the noisy flow data in Figure 18. At similar Reynolds numbers as the HLB and BAM6QT noisy runs, the travelling waves are barely visible under quiet flow and approximately two orders of magnitude smaller than the waves under noisy flow. As the Reynolds number increases, the magnitude of the travelling waves increases, but is still smaller than the amplitude of the travelling waves under noisy flow at lower Reynolds numbers. It is not known how much the difference in wave amplitude is caused by non-linear amplification of the waves or the differing free-stream noise levels.

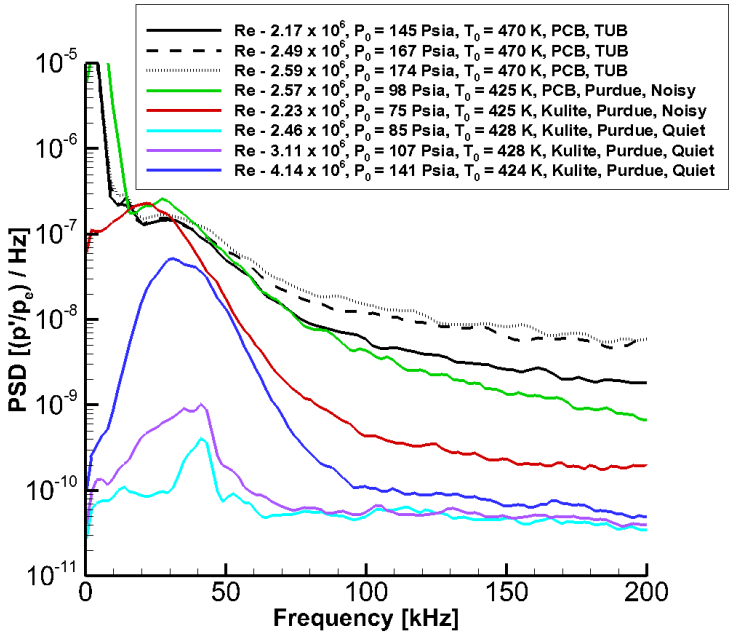

Figure 18. PSD of sensors in the BAM6QT under noisy and quiet flow, and in the HLB. HLB PCB at x = 0.257 m from nosetip. BAM6QT PCB at x = 0.321 m and Kulite at x = 0.362 m from the nosetip.

F. Secondary Instability of Stationary Crossflow Waves

Data has been collected that may show the presence of a travelling secondary instability of the stationary crossflow waves. The secondary instability appears near the point of saturation of the stationary vortices and grows rapidly until breakdown of the waves. Figure 19 shows two TSP images at similar conditions with the smooth and rough Torlon inserts (50 dimples). The red line represents the lee ray, and the Kulite array is 150° from the windward ray and circled. Limiting our focus to near the Kulite array, for the smooth case the stationary vortices are barely visible. When the roughness insert is added, the magnitude of the stationary waves increases greatly near the Kulite array. The waves may be breaking down to turbulence just downstream of the sensors.

The PSD of the Kulite sensor closest to the leeward ray is shown in Figure 20 with both the smooth and rough Torlon inserts. For both cases, the primary travelling crossflow waves are measured near 40–50 kHz. When the roughness insert is added and the stationary waves grow large downstream of the sensors, a second peak in the PSD appears near 150 kHz. This peak may correspond to the travelling secondary instability of the primary stationary waves.

Another set of tests were done to investigate the possible secondary instability. Unfortunately due to time restrictions TSP was not added to the model. The model was equipped with PCB and Kulite sensors 0.36 m from the nosetip at various different azimuthal angles.

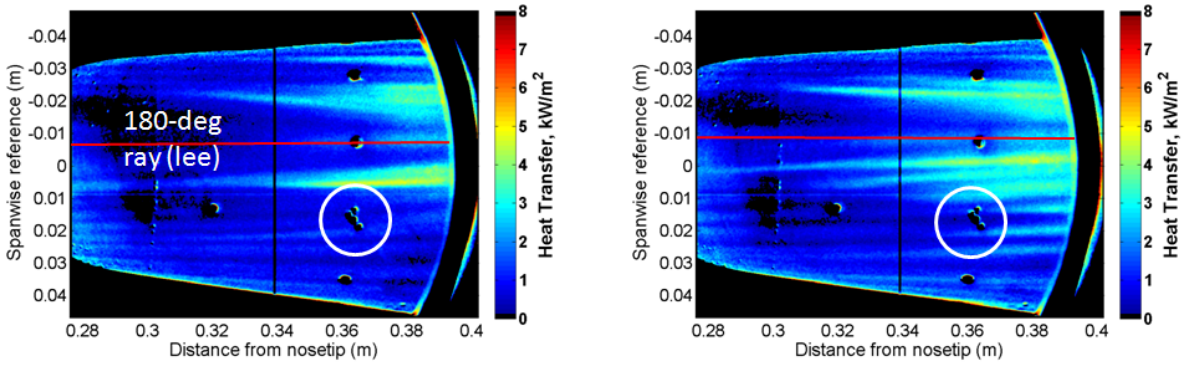

(a) Smooth. $T_{wall} = 300$ K

(b) Roughness insert (50 dimples). $T_{wall} = 300$ K

Figure 19. TSP images with varying roughness inserts under quiet flow. Red line indicates the lee ray (180° from the windward ray), and the Kulite array is 150° from the windward ray (circled in the images). Re = 9.3×10^6/m, P_0 = 140 psia, T_0 = 435 K.

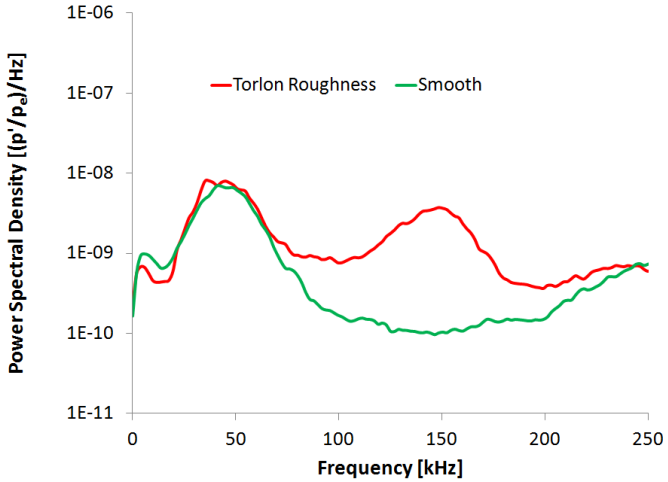

Figure 20. PSD of Kulite sensor circled in Figure 19. Sensor was 0.36 m from the nosetip and 150° from the windward ray. All tests under quiet flow. P_0 = 142 psia, Re = 10.8×10^6/m, T_0 = 425 K.

The initial test was done near the maximum quiet Reynolds number with the sensors spanning 0° to 180° azimuthally from the windward ray. The insert with 50 dimples was used. The PSD of each sensor is shown in Figure 21. The two sensors closest to the leeward ray show a turbulent spectra. The three sensors closest to the windward ray show a laminar spectra, with a slight peak near 300 kHz. This peak may be due to the second-mode instability, but it is unclear since the frequency of the second-mode wave would be expected to decrease when moving towards the lee ray because of the thickening boundary layer, but it does not. The Kulite at 90° shows a very clear peak at approximately 40 kHz, corresponding to the primary travelling crossflow instability. Kulite sensor resonance is seen as a small peak at 300 kHz. Finally, the PCB sensor at 120° shows a large peak near 400 kHz. It was not clear if this peak was due to the second-mode waves, or the secondary instability of the stationary crossflow waves, therefore further testing was conducted. Note that this 400 kHz peak (at 120° azimuthally) has a frequency significantly higher than the 150 kHz peak (at 150° azimuthally) measured in Figure 20. If both of these peaks in the spectra correspond to the secondary instability of the stationary waves, it might be expected that the frequency would be lower nearer to the lee ray where the boundary layer is thicker, which agrees with the data.

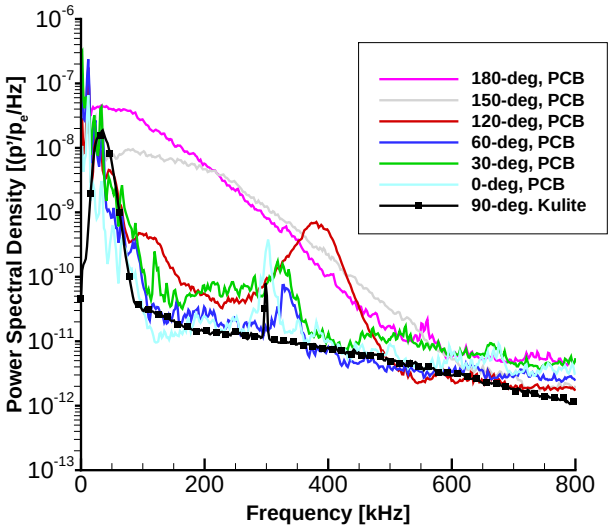

Figure 21. PSD of sensors at 7 different azimuthal locations, 0.36 m from the nosetip during one run, under quiet flow with roughness insert. P_0 = 142 psia, Re = 10.8×10^6/m, T_0 = 425 K.

The sensors were then rotated towards and away from the lee ray by up to 5°, and the PSD of a single PCB is shown in Figure 22 under approximately the same conditions. The red trace at the 120° ray shown in Figure 22 is the same as the red trace in Figure 21. A run under noisy flow showing a turbulent spectra was added as reference. When the sensor was moved to the 117.5° ray (green trace), the spectra is almost identical to the one for the 120° ray case. Moving the sensors to 115° ray (blue trace), the peak near 400 kHz disappears. If the peak in the spectra corresponded to the second-mode instability, it would not be expected that such a small change in azimuthal angle would cause the peak to completely disappear. Moving the sensors to the 121° and 122.5° rays (purple and black traces, respectively), the peak at 400 kHz disappears, but a lower frequency peak near 150 kHz appears. It is not known if the peak at 150 kHz is related to the peak at 400 kHz. This is at a similar frequency as the peak measured in Figure 20 (on the 150° ray). The width of a stationary vortex under similar conditions is between 5 and 10° azimuthally, therefore if the peak at 400 kHz is due to the secondary instability of the stationary waves, it is not surprising that the peak disappears when the sensors are moved ±5°. It is also possible that the pattern of stationary vortices was altered when the cone was rotated because each ray would see a different random roughness, but this cannot be determined without TSP.

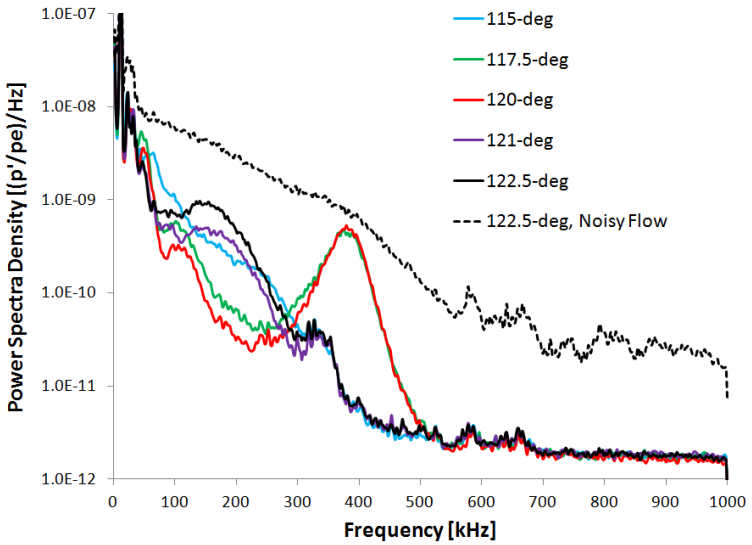

Figure 22. PSD of PCB sensor 0.36 m from the nosetip. Azimuthal angle measured from the windward ray. All tests with roughness insert and under quiet flow. Re = 10.8×10^6/m, P_0 = 142 psia, T_0 = 425 K.

The next set of tests was done to determine how roughness affects this apparent secondary instability. Four tests were done, two with the roughness insert and two with the smooth insert, with the PCB sensor at the 120 and 117.5° rays. Figure 23 plots the PSD the PCB sensor from the four runs. When the roughness is added, the PCB shows a peak near 400 kHz. When the smooth insert is used the peak near 400 kHz disappears. As mentioned, no TSP data was available for these tests, but it is hypothesized that the roughness is producing larger amplitude stationary waves that are breaking down near the sensor, while the smooth case produces smaller stationary waves that break down further downstream.

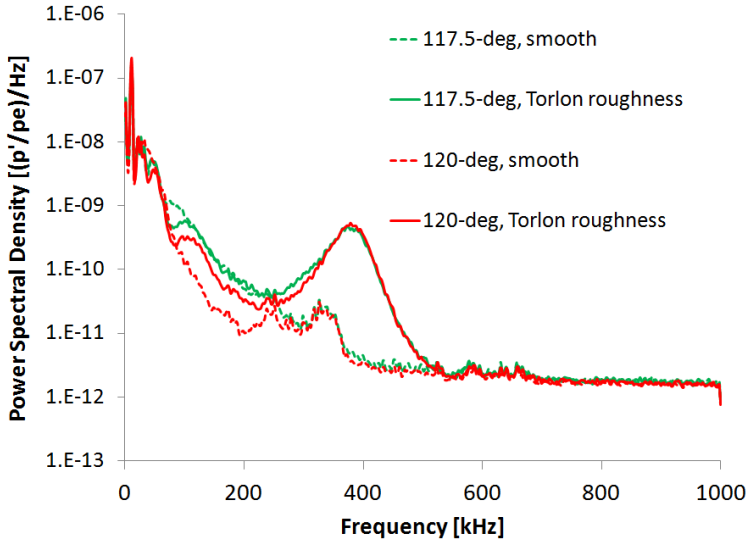

Figure 23. PSD of PCB sensor 0.36 m from the nosetip showing effect of roughness on the high-frequency instability. Azimuthal angle measured from the windward ray. Quiet flow. Re = 11.0×10^6/m, P_0 = 143 psia, T_0 = 420 K.

The repeatability of the data was determined by performing repeat runs with a PCB sensor on the 120° and 115° ray. The PSD is shown in Figure 24. For the 120° ray case, once again a peak in the PSD is seen near 400 kHz and the repeat run also shows a peak at the same frequency with a very similar magnitude. When the PCB is on the 115° ray, the peak at 400 kHz disappears. Thus, the results show good repeatability.

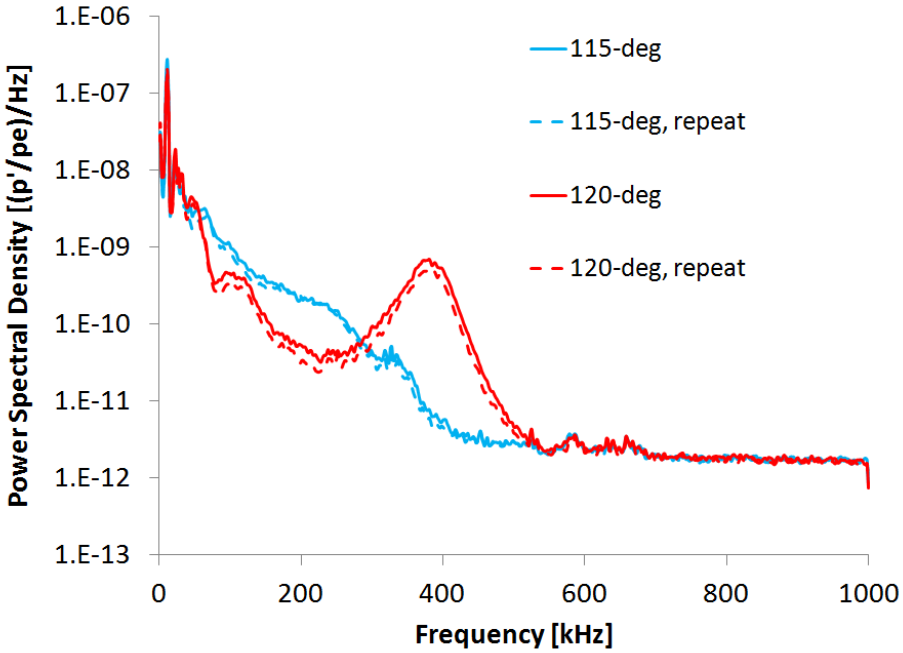

Figure 24. PSD of PCB sensor 0.36 m from the nosetip showing repeatability of measurements. Azimuthal angle measured from the windward ray. Tests with Torlon roughness insert and under quiet flow. $P_0 = 143$ psia, Re $= 11.0\times10^6$/m, $T_0 = 420$ K.

1. *Summary of Secondary-Instability Experiments*

A high-frequency instability, 3–10 times larger than the primary travelling instability, has been measured near the region of stationary wave breakdown. This high-frequency instability may correspond to the travelling secondary instability of the stationary crossflow waves. Tests with a Kulite sensor on the 150° azimuthal ray, 0.36 m from the nosetip, measured an instability near 150 kHz when the stationary waves appeared to begin to break down as imaged by the TSP.

Additional tests measured an instability near 400 kHz on the 120° azimuthal ray, 0.36 m from the nosetip. When the cone was rotated ±5°, the instability was either no longer present or a lower frequency peak (around 150 kHz) appeared. If the 400 kHz peak in the spectra corresponded to the 2nd-mode instability, small changes in azimuthal angle would be expected to cause a slight change in peak frequency (because of the azimuthal variation in boundary-layer thickness), but the instability peak disappears when the sensor is rotated by small angles. It seems likely that the secondary instability of the stationary crossflow waves is being measured. However, computations are needed for confirmation.

IV. Effects of 2-D Roughness on a Flared Cone

A. Brief Background and Previous Experiments

The flared cone was designed to maintain a constant boundary layer thickness; it is ideal for observing large amplitude second mode waves in a narrow frequency band since the second mode wave is highly dependent on boundary layer thickness. In 1959, James[25] found that an optimal roughness height could possibly delay transition on a hollow cylinder. More recent experiments by Fujii[26] at the JAXA 0.5m hypersonic wind tunnel show that a wavy wall roughness applied to a 5° half-angle sharp cone can sometimes delay boundary-layer transition. The cause of this phenomena had not been known at this point. Computations by Duan et. al.[15] suggest the mechanism is related to the location of the roughness relative to the synchronization point. The synchronization point is defined by Wang and Zhong[27] as the location where the dimensionless phase velocities of mode S and F waves are equal. Computations by Fong et. al[28] show that roughness elements that are smaller than the boundary layer thickness and located downstream of the synchronization point for a given frequency can alter the mean flow such that second mode instabilities are damped while lower frequencies are amplified. This could explain the delay in transition that previous experiments have observed after roughness is applied. Experiments by Bountin[29] showed that a wavy wall on a flat plate can be used to help damp the second mode instability through gentle separations and reattachments of the boundary layer creating a parallel mixing layer on the wall. However, Bountin et. al. did not see a clear effect.

B. Current Results

The flared cone was fitted with a 1mm radius nose tip for all the experiments. The roughness design for the flared cone was proposed by Zhong.[30] The present authors did not expect a substantial effect, based on reference 28, but carried out the test in the BAM6QT anyway. Roughness strips were created from layers of high temperature tape. All strips were cut as accurately as possible to the 2.66mm width and then layered twice to provide the desired 0.66mm height. These dimensions correspond to double and half the local boundary-layer thickness, respectively. Table 2 shows the locations of the strips with respect to the nose tip of the model. Table 3 shows the configurations of roughnesses used in testing in order to improve the clarity and brevity of the results. The first four PCB sensors are positioned directly behind roughness strips on the model. It is possible for this to alter some of the data seen in the spectra. The fifth sensor is not located directly behind roughness.

Table 2. Locations of Roughness and Sensors on the Flared Cone.[31]

Roughness Strip	Distance from Nose Tip (m)	Sensor Number	Distance from Nose Tip (m)
1	0.299	PCB 1	0.281
2	0.322	PCB 2	0.332
3	0.350	SB Gauge	0.354
4	0.378	PCB 3	0.409
5	0.405	PCB 4	0.434
6	0.430	PCB 5	0.450

Table 3. Roughness Configurations for Testing on the Flared Cone.[31]

Roughness Configuration	Roughness Strips Added
Roughness 0	1 2 3 4 5 6
Roughness 1	2 3 4 5 6
Roughness 2	3 4 5 6
Roughness 3	4 5 6
Roughness 4	5 6
Roughness 5	1 3 5
Roughness 6	1 4

Figure 25 shows the power spectral density along a single ray on the flared cone without any roughness at a unit Reynolds number of 12.2×10^6/m. Using PCB 131A31 sensors, the dominant peak is centered at 305-310 kHz depending on the downstream location of the sensor. The amplitudes of the peaks do not grow a significant amount along the cone. It seems that the waves are non-linearly saturated. There are additional harmonics centered near 615 kHz and 915 kHz and a marginal peak near 775 kHz. Roughness configuration 0 was then applied and the power spectra can be seen in Figure 26. The second mode peaks are no longer the major disturbance and are concealed by the noise floor of the sensors. Another peak is located around 150-155 kHz. This concurs with the idea that the roughness behind a certain frequency's synchronization point damps the target frequency and amplifies lower frequencies. The furthest downstream sensor (PCB 5) contains the clearest spectra. PCB 5 shows that the power of the rough cone's peak at 155 kHz is roughly an order of magnitude smaller than the smooth cone's second mode peak at 315 kHz. The damping of the second mode was not expected according to the experiment completed by Bountin,[29] since the strips are too far apart for a parallel mixing layer to exist. The design given to us from Prof. Zhong allowed us to observe this phenomena.

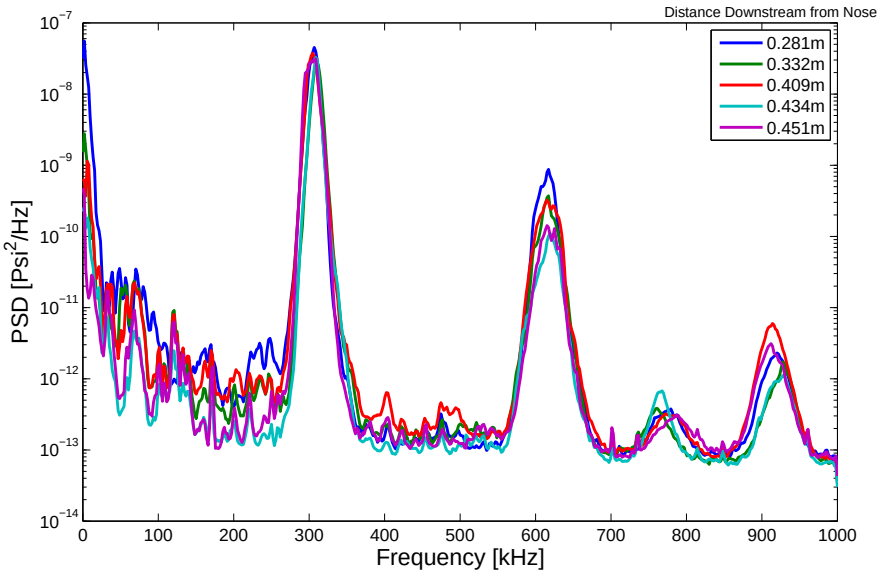

Figure 25. Power spectral density along flared cone without roughness elements, P_0 = 168.7 psia, Re = 12.2×10^6/m, T_0 = 428 K.

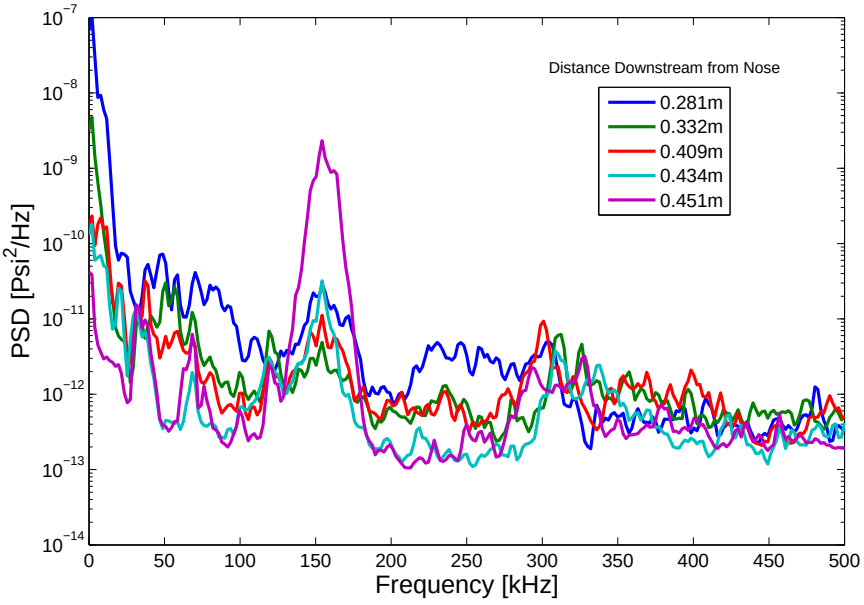

Figure 26. Power spectral density along flared cone with roughness configuration 0, P_0 = 169.3 psia, Re = 12.0×10^6/m, T_0 = 434 K.

Figure 27 shows the TSP images for the smooth and rough cases at a unit Reynolds number of 12.2×10^6/m. In figure 27(a), the smooth case, we start to see heating associated with the saturation and breakdown of the second mode waves, at the very base of the cone. We do not see a heating-cooling-reheating region since the blunter nose tip delays the development of the second mode and subsequent breakdown. For figure 27(b), the rough case, this heating is not present. The boundary layer seems less unstable and the second mode breakdown is not present.

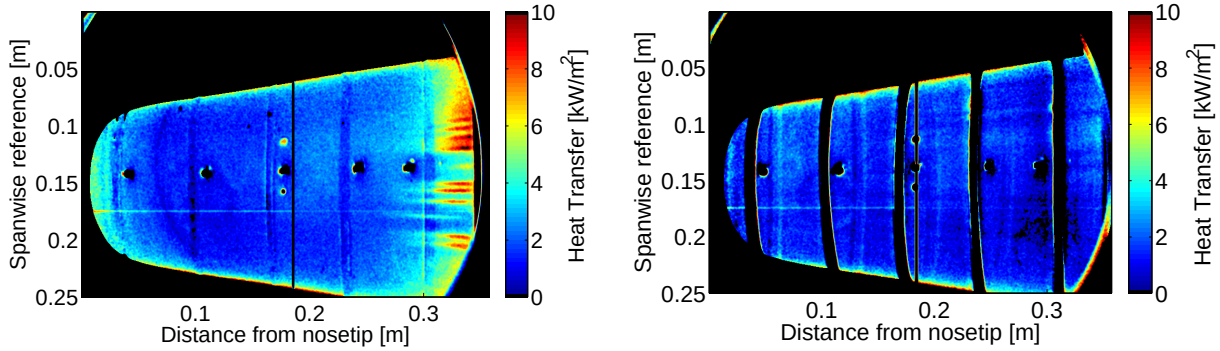

Figure 27. TSP images with roughness configuration 0 applied (a) P_0 = 168.7 psia, Re = 12.2×10^6/m, T_0 = 428 K and (b) P_0 = 170.2 psia, Re = 12.2×10^6/m, T_0 = 428 K.

The effect of Reynolds number on the cone with roughness configuration 0 applied is seen in Figure 28. The low frequency peaks are all near 150 kHz and the amplitudes decrease with the Reynold's number, or stagnation pressure. All the roughness configurations show similar behavior with changing Reynolds numbers. The clearest data occurred at the highest quiet Reynolds number at $P_0 = 170$ psia. The following discussion will focus on these conditions.

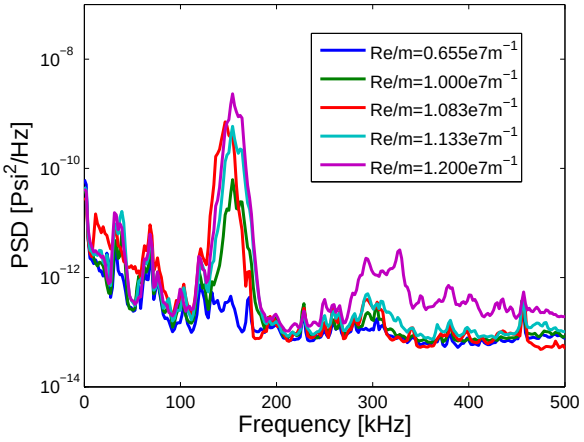

Figure 28. Power spectral density at the furthest downstream sensor with roughness 0 at varying Reynolds numbers.

The farther upstream roughness strips were then removed, one by one, to find the effect. Figure 29 shows the power spectra of the furthest downstream PCB sensor. The damping of the second mode perturbation and the amplification of the lower frequency is greatest for the case where the roughness is closest to the nose tip (Roughness 0). As the roughness moves downstream, the damping and the amplification decrease. This supports Duan[15] and Fong,[28] who stated that the damping is related to the distance between the roughness and the synchronization point. For the flared cone the synchronization point is located around 0.25 m from the nose tip. Every time a roughness was removed the initial strip is further away from the synchronization point. Figure 30 shows the TSP results for roughness arrays 1 and 4. There are no streaks of heating along the entire body of the cone. Roughness 2 and 3 also lack streaks of heating.

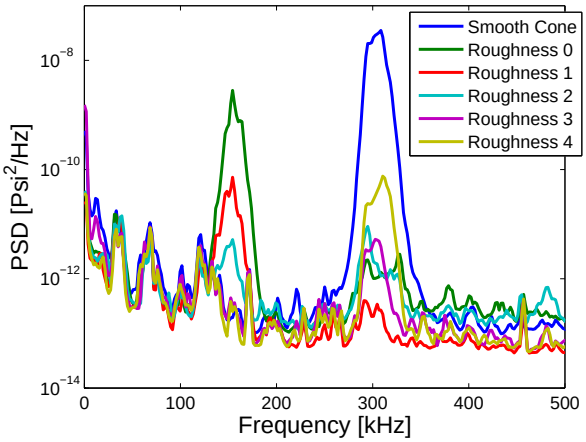

Figure 29. Power spectral density at the furthest downstream sensor for different initial roughness locations (configurations 0-4) , $P_0 = 170.0 \pm 1.4$ psia, Re $= 12.2 \pm 0.4 \times 10^6/\text{m} \pm 0.1 \times 10^6/\text{m}$, $T_0 = 428.2 \pm 4$ K.

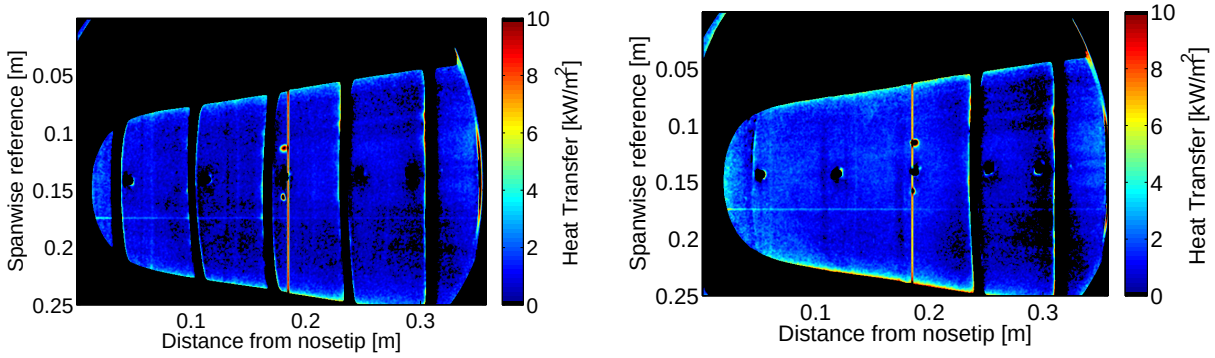

Figure 30. TSP images with roughness configurations 1, 4 respectively (a) P_0 = 169.2 psia, Re = 12.4×10^6/m, T_0 = 425 K and (b) P_0 = 171.4 psia, Re = 12.1×10^6/m, T_0 = 436 K.

The effects of changing the spacing between each strip was then tested, as shown in Figure 31. For both spacing cases, the strip closest to the nose tip remained, in order to avoid effects from moving the initial roughness location. Roughness array 5 featured 5.1 cm spacing between the strips and roughness array 6 featured 7.9 cm. The power spectra show that the wider spacing managed to significantly damp the second mode disturbance at 310 kHz, while not amplifying any lower frequencies. This provides the largest change in the amplitudes of the major disturbances present in the spectra. Figure 32 shows that heating streaks are present in between the last roughness strip and the base of the cone. The cause of these streaks is not known. For all the testing with roughness applied, these are the only cases with heating streaks present. It is possible that these streaks are induced by the Görtler instability.

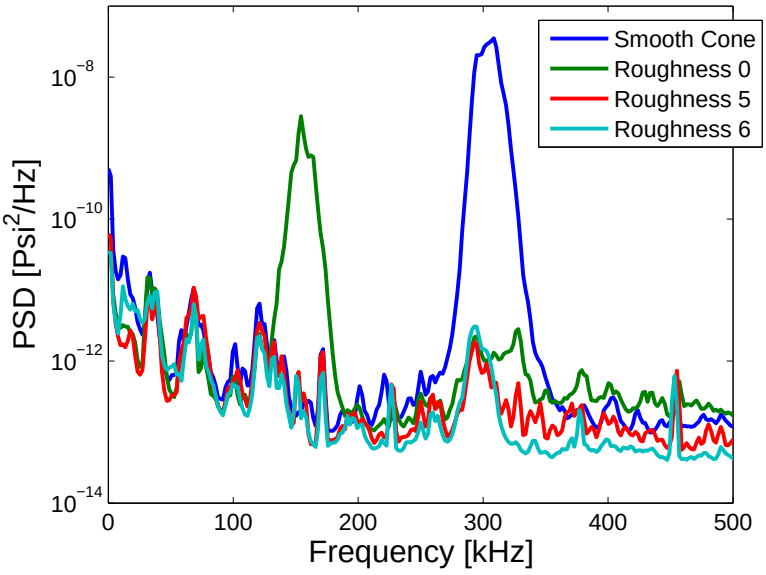

Figure 31. Pressure spectra at the furthest downstream sensor with varying roughness strip spacing. Roughness 0 contains the smallest spacing and Roughness 6 contains the widest. P_0 = 169.5±0.7 psia, Re = 12.2×10^6/m, T_0 = 429±2 K.

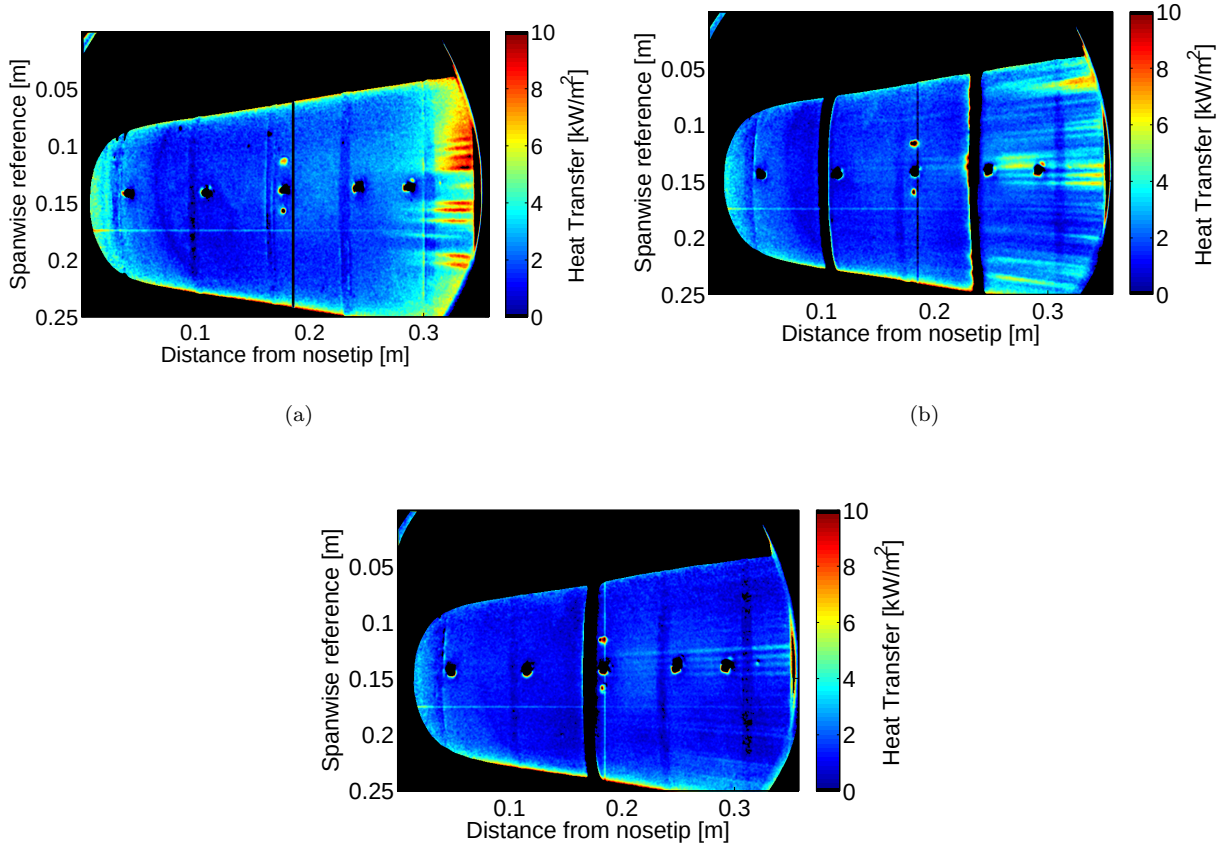

(a)

(b)

(c)

Figure 32. TSP images with roughness configurations 0, 5, 6 respectively (a) Roughness 0, P_0 = 168.7 psia, Re = 12.2×10^6/m, T_0 = 428 K, (b) Roughness 5, P_0 = 169.2 psia, Re = 12.1×10^6/m, T_0 = 431 K, and (c) roughness 6, P_0 = 170.0 psia, Re = 12.2×10^6/m, T_0 = 429 K.

V. Entropy-Layer Instability Measurements on Cone-Ogive-Cylinder Models

Boundary-layer transition is particularly important in hypersonic flight. Heat transfer increases by three to eight times requiring more thermal protection. Forces and moments also change significantly, affecting vehicle control authority. However, hypersonic transition is extremely complex with additional instabilities and parametric influences that are not a factor at subsonic speeds.[32]

Experimental measurements are required to understand which mechanisms induce transition under different conditions. A better understanding of the physics behind these instabilities will help develop mechanism-based prediction methods.[33–35]

A. Introduction and Previous Work

In supersonic flow, variations in the strength of a shock along its length create large temperature and velocity gradients normal to the streamlines. These high gradient areas make up the entropy layer and can affect the downstream flow characteristics close to the body.[36] Entropy-layer effects are particularly important for

blunt objects that have large strength variations along the shock.[37]

Entropy layers, like boundary layers, can have a generalized inflection point in the angular momentum. This inflection point meets the necessary condition for instabilities to be present in the entropy layer.[38,39] Entropy-layer instabilities are an inviscid phenomenon and the most amplified waves are not necessarily oblique.[40] Multiple experiments have hypothesized that the interaction of the entropy layer with the boundary layer may significantly affect the transition Reynolds number.[40–46]

Stetson et al. measured entropy-layer instabilities over a blunt cone using hot wire anemometry. They discovered that the entropy-layer disturbances grew slowly outside the boundary layer, diminished slightly as they entered the boundary layer, and then proceeded to grow rapidly inside the boundary layer.[47] Lysenko performed similar measurements over a flat plate with a blunt leading edge.[45]

Measurements of entropy-layer instabilities were previously made in the BAM6QT with several cone-ogive-cylinder configurations using Kulite pressure transducers and hot-wire anemometers. The surface measurements show an instability magnitude that increases, then decreases, and eventually increases rapidly. This may be due to the entropy-layer entering the boundary layer. Off-surface measurements using hot wires show the instability grow and approach the model as it moves downstream. These preliminary results showed that the frequency and magnitude of the measured instability is dependent on the nosetip used.[48,49]

Additional hot-wire and surface measurements were performed using an array of cone-ogive-cylinder configurations. The data provide details about the location, magnitude, and width of the entropy-layer instability and how these characteristics vary with a change in the nosetip angle. Cross-correlations of hot-wire and surface measurements confirm that they are measuring the same instability, and provide additional understanding of its characteristics.[50]

B. Computational Setup

The mean flow was calculated using a code developed at the University of Minnesota, Stability and Transition Analysis for Hypersonic Boundary Layers (STABL). STABL is a two-dimensional/axisymmetric, Navier-Stokes solver that uses implicit Data-Parallel Line Relaxation (DPLR).[51] The mean-flow computations were made for each design under BAM6QT operating conditions and compared with experimental measurements. Stability analysis of the entropy layer was not completed because the STABL configuration at Purdue is not currently set up to compute instabilities outside the boundary layer.

C. Experimental Setup

The cone-ogive-cylinder design consists of a sharp cone that tapers into an ogive-cylinder. The shape of the cone-ogive forebody dictates the shape of the shock, and thereby dictates the entropy-layer characteristics. The experimental model is shown in Figure 33 with four of its nosetips. It consists of a 5-cm diameter cylinder that is 0.86 meters long, and 8 detachable cone-ogive nosetips with cone angles ranging from 25 to 40 degrees. The profiles are shown in Figure 34.

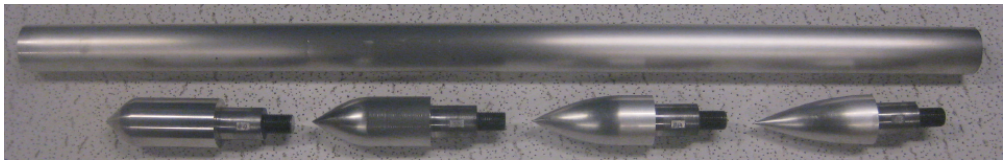

Figure 33. Photo of Cone-Ogive-Cylinder Model with Interchangeable Cone-Ogive Sections

The cone-ogive-cylinder model and the interchangeable nosetips were fabricated in the Purdue machine shop. They were made of 6061-T6 aluminum. With the nosetip attached, the model has a total length of 94 cm. A previous cone-ogive-cylinder model was used in initial experiments. When the new model has the 30-degree nosetip installed, the two models have the same dimensions.

A majority of measurements were made with the 30 to 35-degree nosetips because they provided the best entropy-layer instability data. Hot-wire measurements using the 25-degree model showed no evidence of an

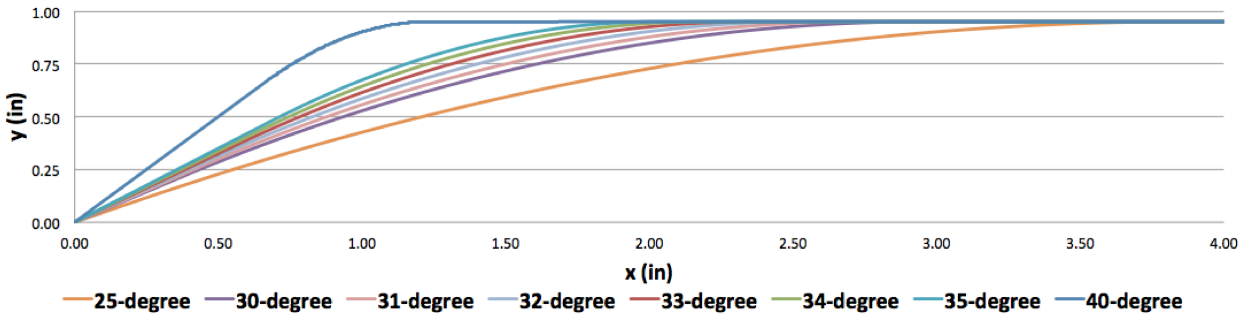

Figure 34. Profiles of all eight cone-ogive-cylinder leading-edge configurations.

entropy-layer instability. The 40-degree model was difficult to start in the tunnel and the resulting data were suspect. A picture of all eight interchangeable nosetips is shown in Figure 35.

Figure 35. Picture of all eight interchangeable cone-ogive portions of the cone-ogive-cylinder model.

Figure 36 shows the pressure transducer port locations. Kulite XCQ-062-15A pressure transducers were installed in these ports, flush with the model surface, to measure surface pressure fluctuations. The ports were machined in the cone-ogive-cylinder at 8 axial locations ranging from 0.52 to 0.86 meters. An additional port was machined at the 0.56-meter location with the two holes azimuthally separated by 0.25 centimeters, measured from the port centers.

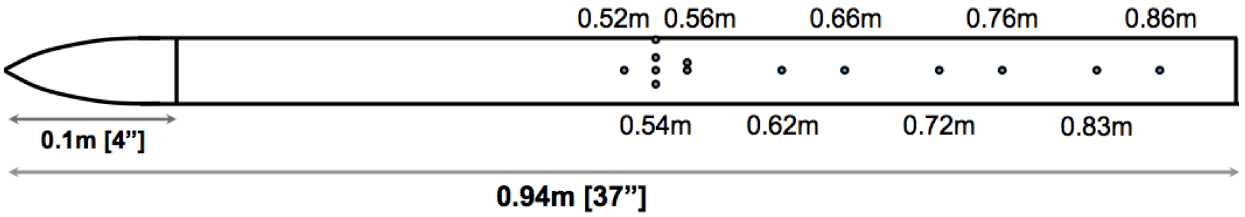

Figure 36. Sketch of the new cone-ogive-cylinder model with surface sensor locations labeled.

The four surface sensor ports at 0.54 meters were added later than the other ports. They were placed at different azimuthal locations. One of these sensors was inserted along the same line as the other surface sensors and the other three were drilled at -90, -15, and 25 degrees from this center hole. Figure 37 shows a picture of the three sensors closest to the centerline. Also shown in this picture is the sensor at x = 52 cm and the two sensor ports at x = 56 cm.

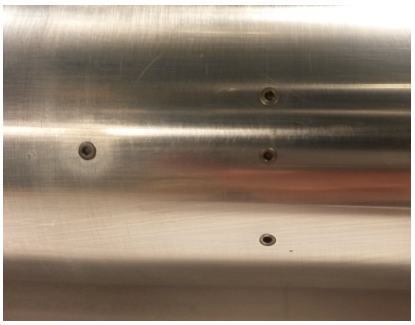

Figure 37. Picture of Kulite pressure transducers at x = 52 and 54 cm as well as two open sensor ports at x = 56cm.

1. Hot-Wire Anemometer

Off-surface measurements were made using 0.0002-inch diameter Platinum-Rhodium Wollaston hot wires with an overheat ratio near 1.[52] They provide excellent spatial resolution due to their extremely small size. This resolution was important in the entropy-layer measurements due to the small radial span of the entropy-layer.

Hot-wire probes were placed at a specific axial location for each run, then traversed in small radial increments during the run to measure disturbances above the surface of the model. A close-up picture of one of the hot-wire probes is shown in Figure 38. The hot-wire probes used in this research were built by Jim Younts at Purdue University.

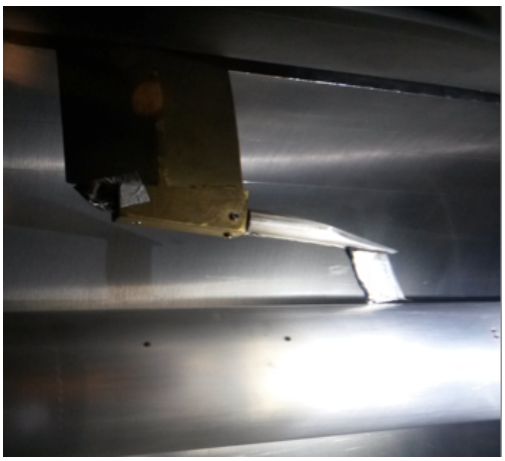

Figure 38. Picture of the hot wire probe installed inside the BAM6QT and held directly over the surface of the cone-ogive-cylinder.

Figure 39 shows an image of the digital oscilloscope screen after a typical hot-wire measurement. The blue line in the figure shows the distance of the hot wire from the model surface. In most runs, including the one shown here, the hot wire started and ended the run about 0.3 millimeters from the model surface. This close proximity reduces the risk of breakage during tunnel startup and shutdown.

The green and purple lines in Figure 39 are the hot-wire ac and dc voltage traces respectively. The dc trace (purple line) shows the increase in mass flux as the hot wire crosses the entropy layer. Near the center of the screen, as the hot-wire probe is about 10 millimeters off the model surface, there is an rapid increase in the voltage measured by the constant-temperature anemometer (CTA). This increase corresponds to the high mass-flux gradients in the entropy layer. It is also at this location, just past the center of the screen,

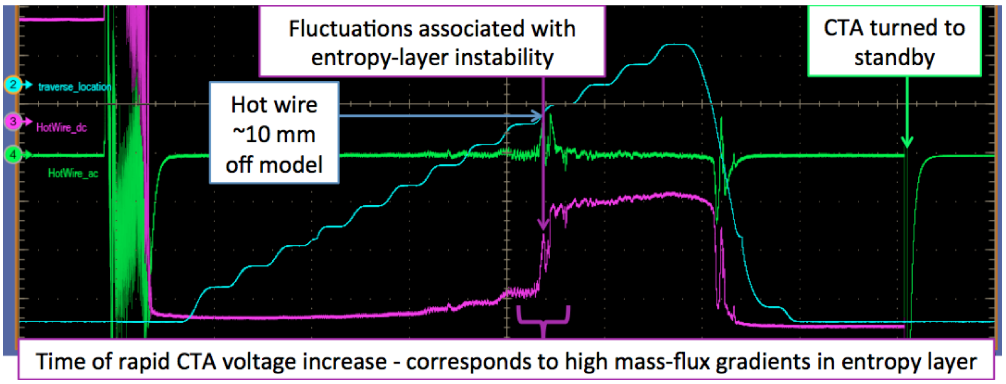

Figure 39. Image of hot-wire voltage traces on the digital oscilloscope screen after measurements over the 30-degree cone-ogive-cylinder at x=52 centimeters (Run 1435).

that the hot wire measures the fluctuations that show the entropy-layer instability. About a second later the hot wire probe is moved back towards the model surface and the decrease in mass flux and instability fluctuations are momentarily visible as the probe passes this same vertical location. Shortly after the hot wire is placed near the surface, the hot-wire signal drops off the screen. This happens as the anemometer is turned to standby in preparation for tunnel shutdown.

D. Computational Results

Computations of the mean flow yielded the angular momentum profiles shown in Figure 40. Each case shows a generalized inflection point. The inflection points are shown by local maxima in the profile curves. The inflection points for the plotted profiles range from about 6 to 9 millimeters off the surface. This is outside of the predicted boundary-layer thickness of 4 to 6 millimeters. The generalized inflection point is one indicator of the stability of the entropy layer. Where there is a local maximum, there is the possibility of an instability growth.[38,39]

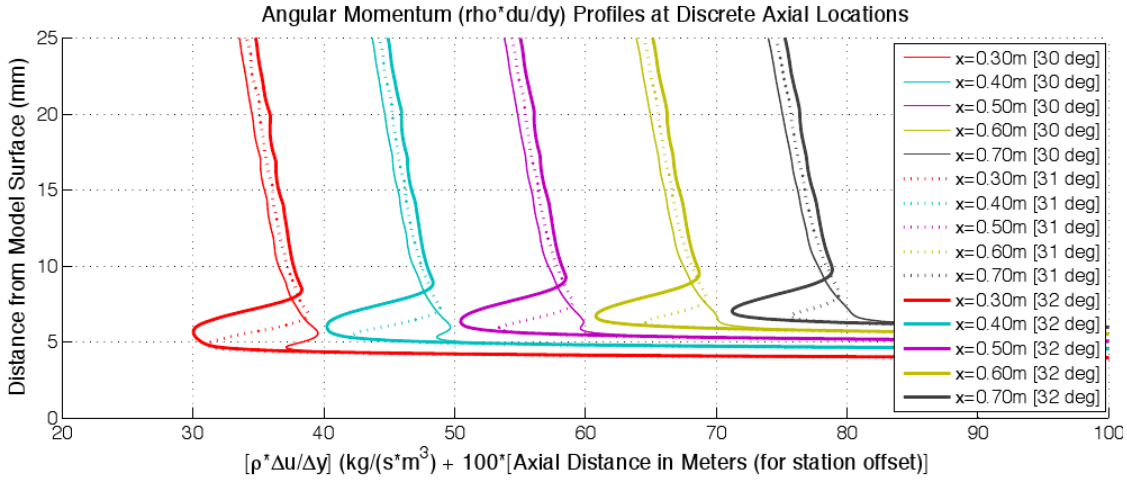

Figure 40. Calculated angular momentum profiles for the 30, 31, and 32-degree cone-ogive-cylinder configurations.

E. Experimental Results

1. *Surface Measurements*

Previous surface measurements on the 30-degree cone-ogive-cylinder showed an increase, then a decrease, and finally a rapid increase in instability magnitude. They also showed that the frequency and magnitude of the measured instability is dependent on the nosetip used.[49] This growth and decay can also be shown by calculating the variation of the root mean square (RMS) amplitude with downstream location. Figure 41 shows the RMS calculated for several different tunnel entries using the two 30-degree models. It shows that the measured instability grows, decreases, then grows again. The spectra were integrated over the amplified frequency band between 10 and 50 kHz.

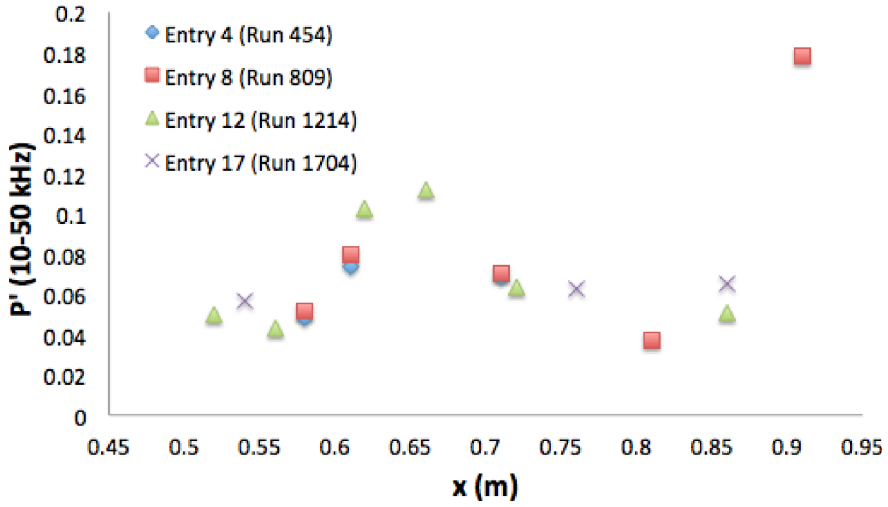

Figure 41. RMS Amplitude vs axial location on the 30-degree cone-ogive-cylinder [data taken from runs 454, 809, 1214, and 1704 with Re/m= $9.3 * 10^6, 9.2 * 10^6, 9.1 * 10^6$, **and** $8.4 * 10^6$ **respectively].**

The highest-magnitude RMS value is at 0.91 meters and was only measured during Entry 8. There was no sensor at that location during Entry 4 and the new model configuration only has sensor ports up to 0.86 meters. To increase confidence in that measurement, the RMS was calculated at similar Reynolds numbers during four different runs in Entry 8. Table 4 compares those RMS values with Reynolds number. The calculated RMS at 0.91 meters shown in Figure 41 is consistent with the values calculated for each run. The RMS increases rapidly as the unit Reynolds number increases from 9×10^6/m.

Figure 42 plots the RMS amplitude against the axial location for the 30 to 35-degree configurations. This figure also shows that in general, as the nosetip angle increases, there is also an increase in instability magnitude at the last measurement location.

The nosetip angle also affects the frequency of the measured instabilities. The power spectra measured on the surface at 52 cm is shown in Figure 43. Each configuration measures distinct instability peaks. As the nosetip angle increases, the frequency of the measured instability decreases.

Table 4. Variation in RMS during Entry 8 on the original cone-ogive-cylinder at 0.91 meters.

Reynolds Number (1/m)	RMS (P'/Pmean)	Run
$8.7 * 10^6$	0.093	822
$8.8 * 10^6$	0.114	822
$9.0 * 10^6$	0.109	810
$9.1 * 10^6$	0.161	809
$9.3 * 10^6$	0.155	810
$9.5 * 10^6$	0.238	809
$10.2 * 10^6$	0.204	823

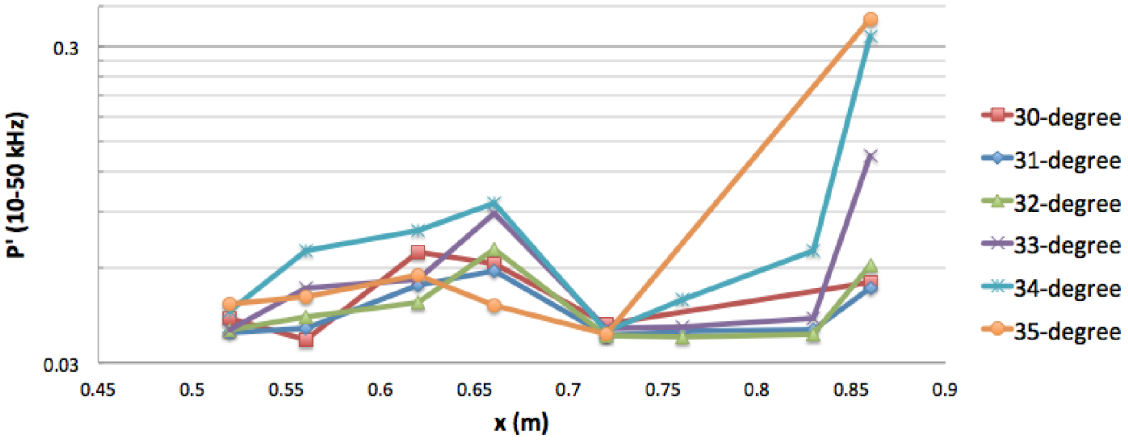

Figure 42. Comparison of the RMS Amplitude vs axial location for each of the cone-ogive-cylinder configurations [data taken from runs 1213, 1522, 1516, 1510, 1503 and 1219 with Re/m= $7.4 * 10^6, 7.8 * 10^6, 7.7 * 10^6, 7.6 * 10^6, 7.7 * 10^6$, **and** $6.8 * 10^6$ **respectively].**

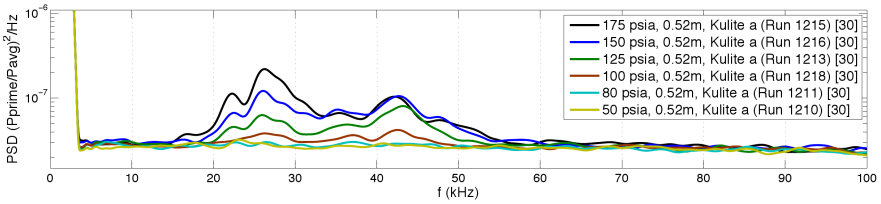

(a) Surface measurements on 30-degree configuration at x=52cm.

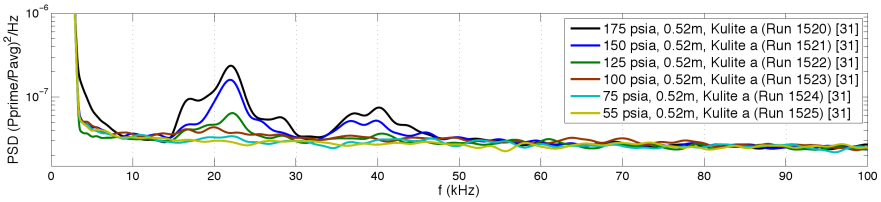

(b) Surface measurements on 31-degree configuration at x=52cm.

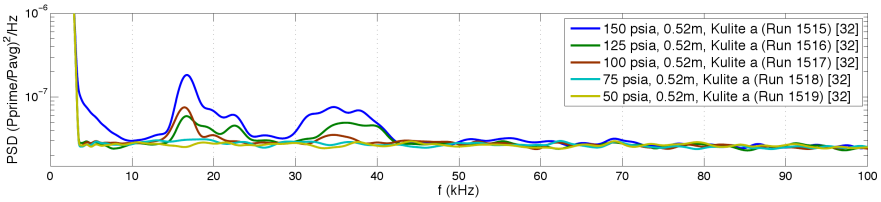

(c) Surface measurements on 32-degree configuration at x=52cm.

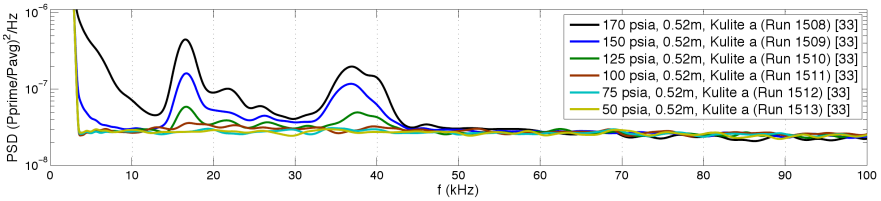

(d) Surface measurements on 33-degree configuration at x=52cm.

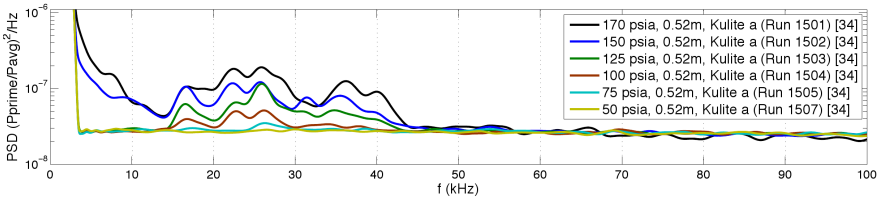

(e) Surface measurements on 34-degree configuration at x=52cm.

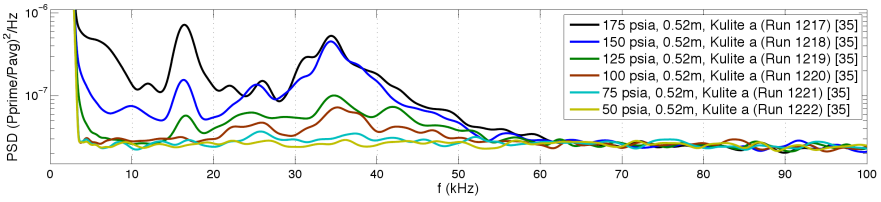

(f) Surface measurements on 35-degree configuration at x=52cm.

Figure 43. Power Spectra of surface measurements at 52cm for the 30 to 35-degree cone-ogive-cylinder configurations.

2. Hot-wire Measurements

Previously-published hot-wire measurements showed the instability grow and approach the 30-degree cone-ogive-cylinder as it traveled downstream.[49] Hot-wire measurements show that as the cone angle increases, the instability magnitude increases. Higher-angle nosetips also resulted in the instability approaching the model at earlier axial locations.

The power spectra for the hot-wire sweeps at three axial locations above the 32-degree cone-ogive-cylinder are shown in Figure 44. The first axial location is at 52 centimeters downstream. The amplified frequencies at this location are shown in Figure 44(a). They show up as very small peaks at frequencies just over 20 kHz when the hot wire was about 10 millimeters above the model surface. As the instability proceeds downstream, its magnitude increases significantly from the 52-centimeter location. Figure 44(b) shows the power spectra at 56 centimeters and Figure 44(c) shows the power spectra at 62 centimeters. At 62 cm, the instability is at the edge of the predicted boundary layer.

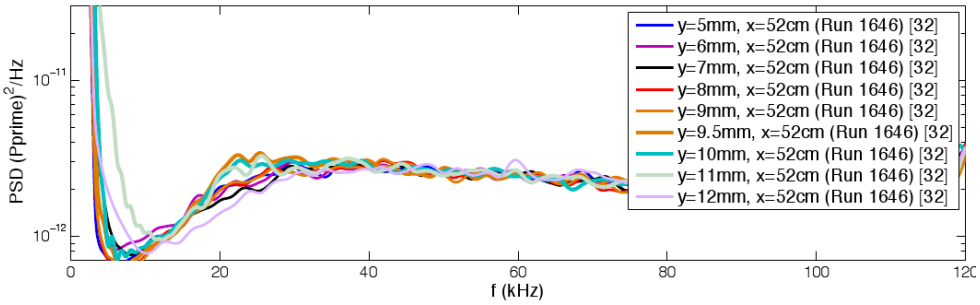

(a) Hot-wire PSD above the 32-degree model at x=0.52m, P0=120psia.

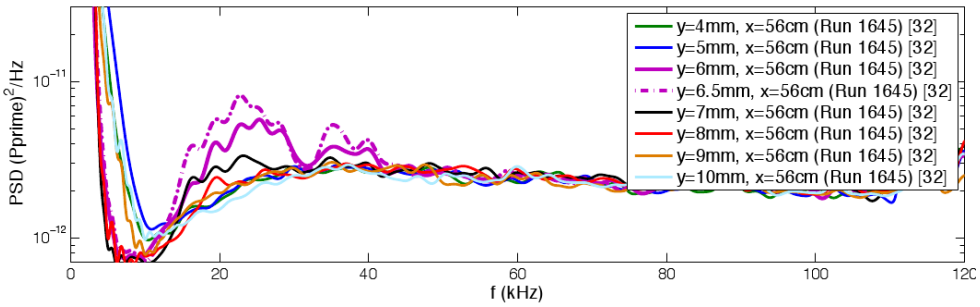

(b) Hot-wire PSD above the 32-degree model at x=0.56m, P0=120psia.

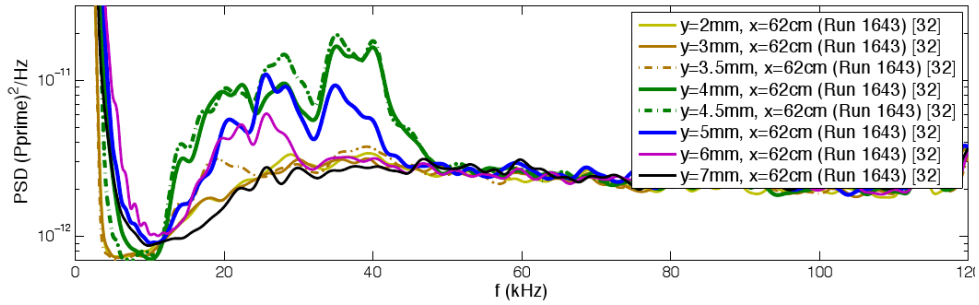

(c) Hot-wire PSD above the 32-degree model at x=0.62m, P0=120psia.

Figure 44. Power spectra from hot-wire measurements above the 32-degree cone-ogive-cylinder at several axial locations showing the instability grow in magnitude and approach the model as it proceeds downstream.

Figure 45 shows the locations where the instability is measured using the 30 and 35-degree nosetips. The green dots in the figure show many of the locations where hot-wire measurements were taken. The red dots indicate the location of the maximum measured instability at a given axial location. These measurements show that as the nosetip angle increases, the axial location at which the instability approaches the model decreases.

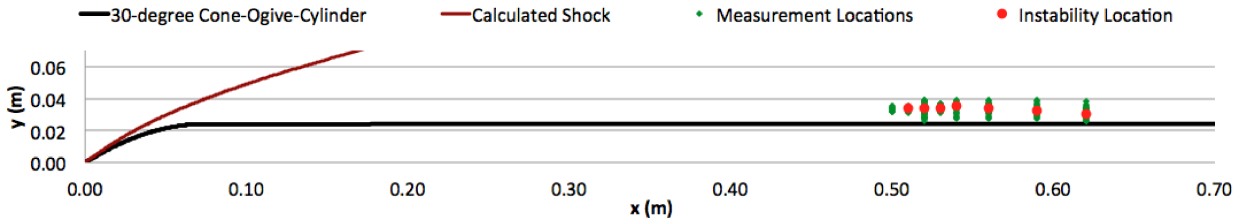

(a) Location of entropy-layer instabilities off the 30-degree cone-ogive-cylinder.

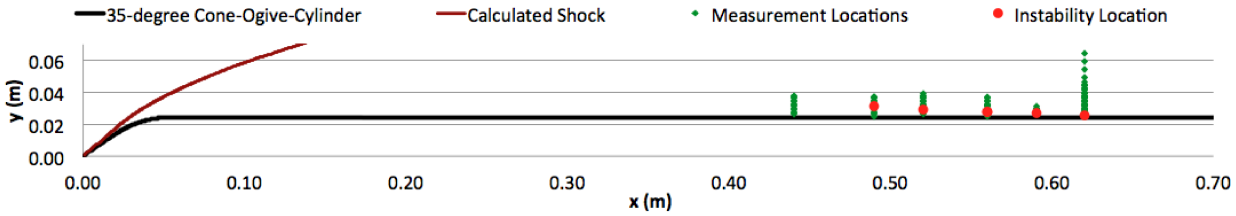

(b) Location of entropy-layer instabilities off the 35-degree cone-ogive-cylinder.

Figure 45. Diagrams showing the locations of measured entropy-layer instabilities off the surface of each of the cone-ogive-cylinder configurations.

The 30 and 35-degree configurations are the two extremes of the majority of the hot-wire measurements taken. For each, the instability approaches the model with downstream distance, but the instability is much closer to the model for the configuration with the bigger nosetip angle. The instability was also measured at an earlier axial location (0.48 meters) with the 35-degree nosetip than with the 30-degree nosetip.

The distance of the maximum instability from each of the cone-ogive-cylinder configurations is shown in Figure 46. The measurements using each nosetip show the instability approaching the model as it proceeds downstream. It also shows that the instability is closer to the model for nosetips with a larger cone angle.

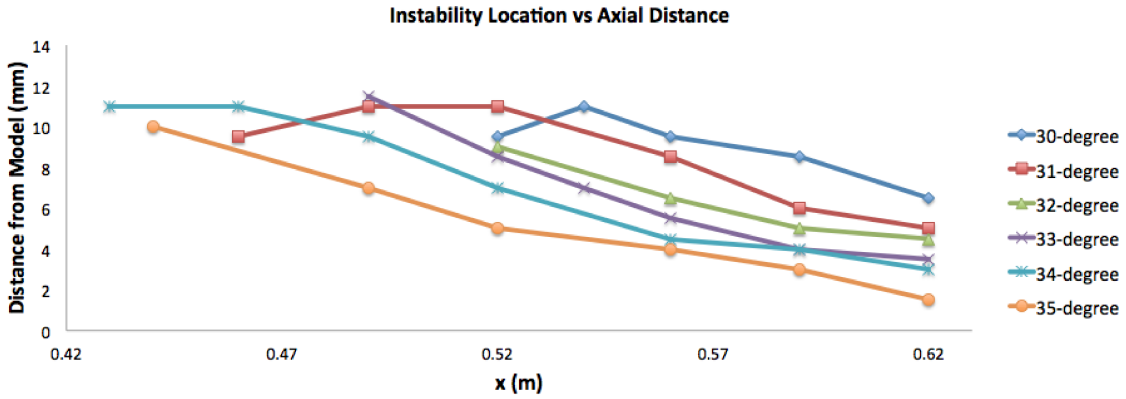

Figure 46. Plot showing the locations of measured entropy-layer instabilities off the surface of the 30 to 35-degree cone-ogive-cylinder configurations.

3. *Measurement Repeatability*

The location and relative magnitude measurements of the entropy-layer instability were very repeatable. Figure 47 shows the spectra for hot-wire measurements above the 32-degree cone-ogive-cylinder at 62 centimeters. The solid lines show the spectra from measurements taken in January 2014 and the dashed lines are from measurements made in March of the same year. Both measurements show the instability reach a maximum at 4 millimeters from the surface. The same frequencies are amplified in each case. This repeatability is typical of the repeatability in all cases.

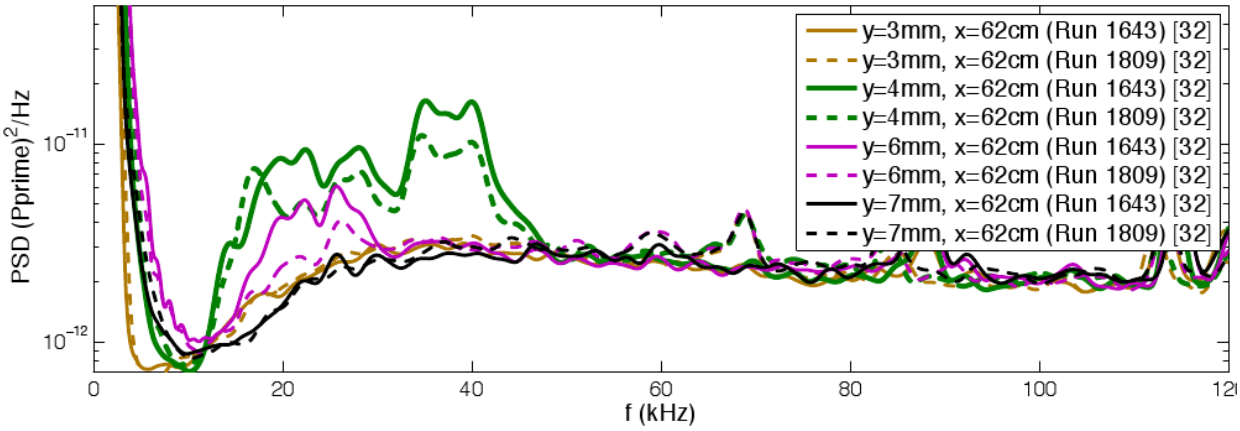

Figure 47. Comparison of Spectra from Hot-Wire Measurements off the surface of the 32-degree cone-ogive-cylinder at x=62cm.

4. *Cross-Correlation of Hotwire and Kulite Surface Measurements*

Cross-correlations were made between the signals measured by the hot wire and the surface Kulites. These correlations show that the instability that is being measured off the model surface by the hot wire is the same one that is being measured at the model surface with the pressure sensor.

Figure 48(b) shows an example of the coherence between the surface Kulite and the hot-wire measurements. The coherence is calculated for data obtained with the hot wire at several distances from the model surface, starting at 3 millimeters, and ending at 9 millimeters.

The calculated coherence depends on the instability magnitude and the distance between the sensors. Coherence values over about 0.2 at a given frequency were considered sufficient to show some correlation between the signals at that frequency.

These calculations clearly show that above and below the location where the instability is measurable by the hot wire, there is very little coherence between the two signals. However, at those locations where the hot wire measures the instability, there is a significant coherence between the surface and off-surface measurements. The coherence in this figure reaches a maximum when the hot wire is about 6 to 7 millimeters off the model surface. This is the same location where the instability magnitude is the greatest.

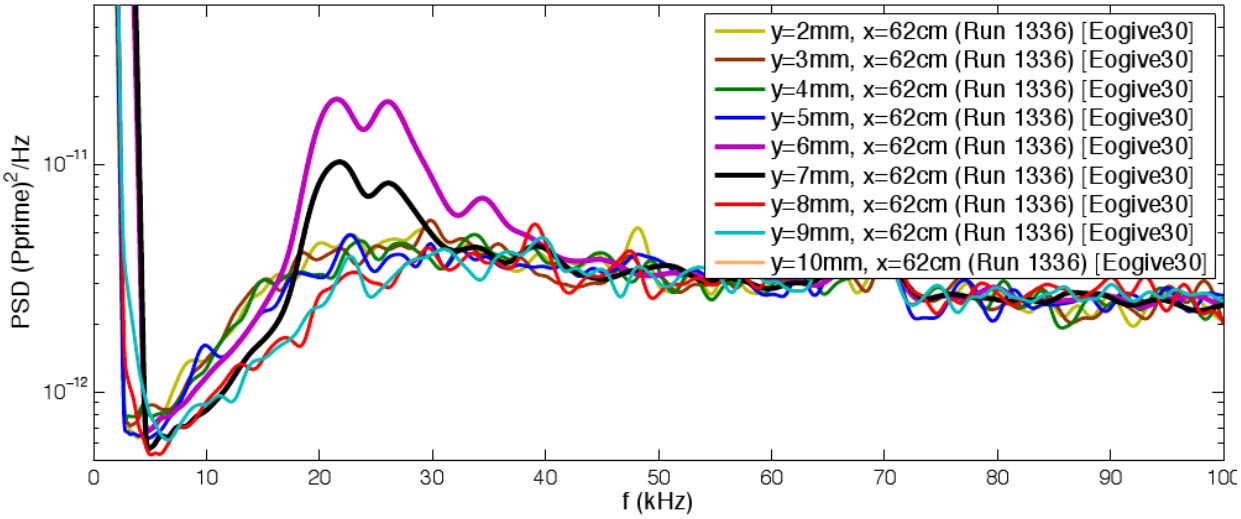

(a) PSD of hot-wire measurements above the 30-degree cone-ogive-cylinder at 62 cm.

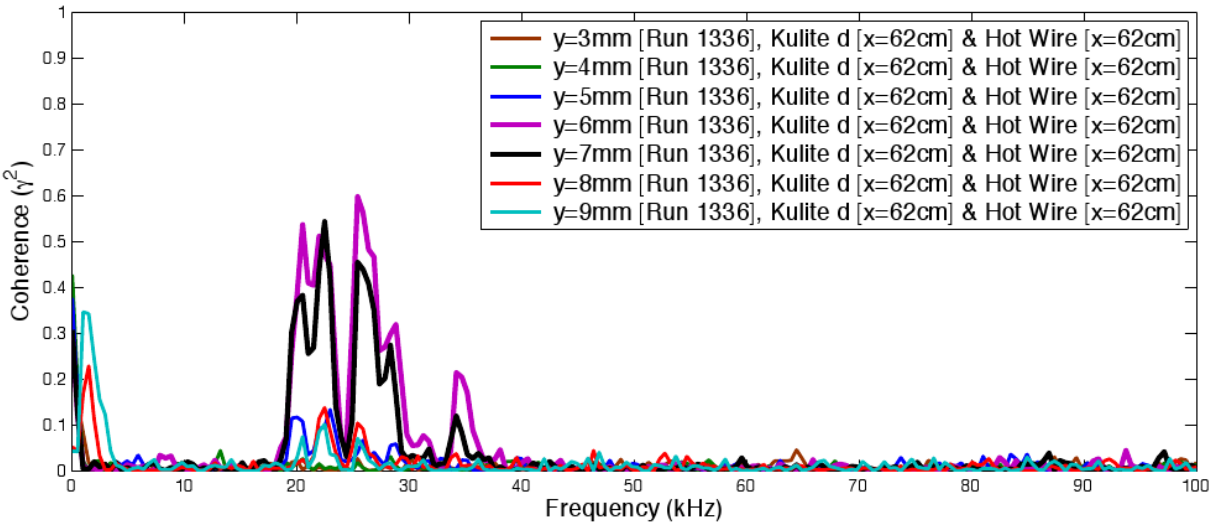

(b) Coherence between Hot-Wire and Surface Measurements (Run 1336).

Figure 48. Power spectra of the hot-wire measurements and their coherence with surface measurements for Run 1336.

5. *Cross-Correlation between Kulite Surface Measurements*

Measurements from the azimuthally-displaced surface sensors shown in Figure 37 were cross correlated to determine if the entropy-layer instability is predominantly two or three-dimensional. The coherence of various pairs of these measurements is shown in Figure 49. It shows the expected decrease in signal coherence as the distance between the sensors is increased.

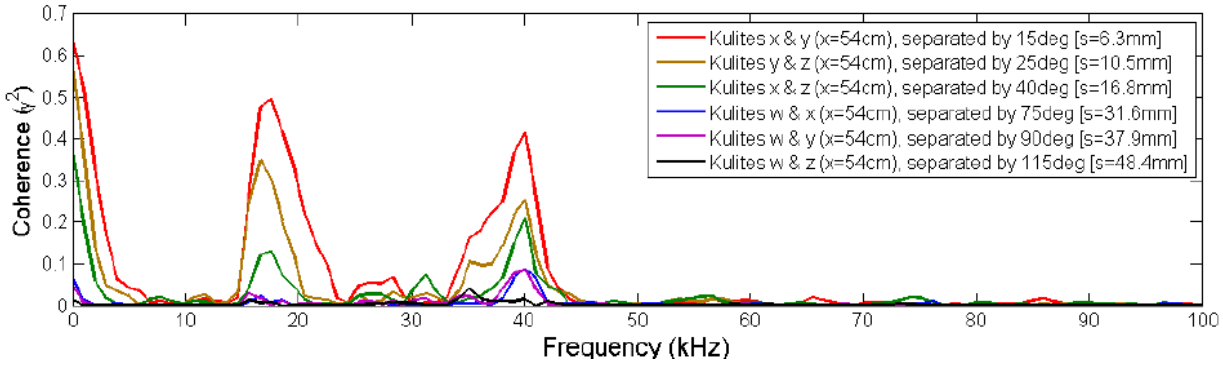

Figure 49. Coherence between azimuthally-displaced surface Kulites at x=54cm (Run 1707, 32-degree cone-ogive-cylinder).

Figure 50 shows the actual normalized correlation values between three pairs of these sensors. All three correlation pairs show a maximum at time zero, indicating a two-dimensional instability. The time between the peak at zero and the next peak is also indicated on Figure 50. This time corresponds to a frequency of about 18 kHz. This is the same frequency found in the power spectra and the coherence (shown in Figure 49).

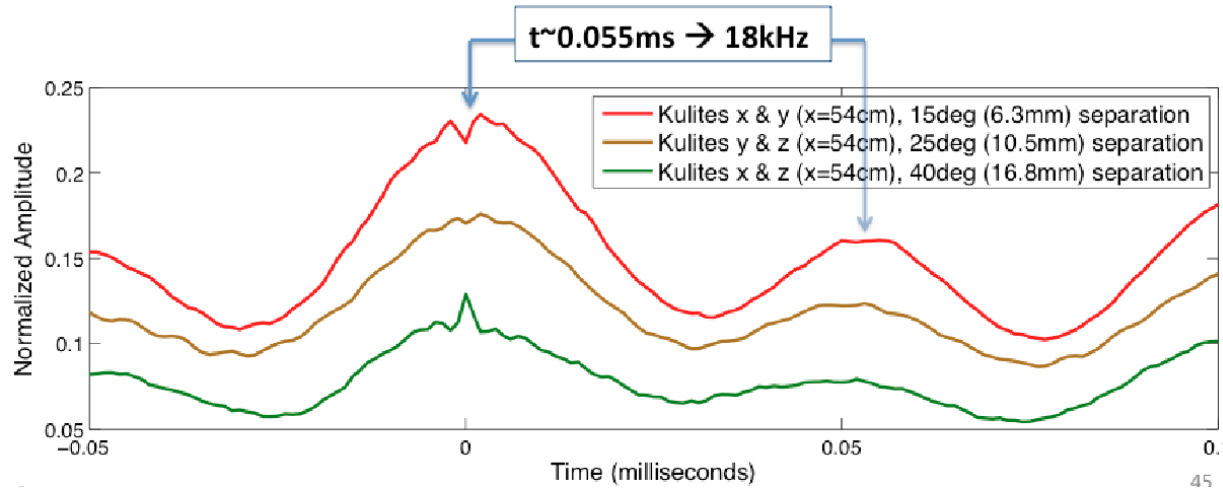

Figure 50. Close-up look at the cross correlation of the azimuthally-displaced surface Kulites (Run 1707, 32-degree cone-ogive-cylinder).

VI. Conclusions

1. A new method for creating arrays of discrete roughness elements was developed and tested on a flared cone at Mach 6. Roughness elements 254 μm in height were found to interact with the second mode waves without becoming a boundary layer trip. When the height of the roughness element was increased to 381 μm, a different streak pattern occurred, and the array still did not act as a boundary layer trip. Further testing with different roughness elements is ongoing.

2. Experiments were performed with a cone at angle of attack looking at crossflow-induced transition. It was found that when small roughness was added near the neutral point of the stationary waves, the generation and breakdown of the stationary waves was significantly altered. The travelling crossflow waves were measured under both noisy and quiet flow, and the wave properties were determined with an array of Kulite sensors. The frequency and wave propagation angle agreed well with computations by Texas A&M and experimental work in the TU Braunschweig Mach-6 tunnel (HLB). When the BAM6QT was run noisy, the amplitude and frequency of the travelling waves agreed well with the HLB data. Under quiet flow in the BAM6QT, the amplitude of the travelling waves was up to several orders of magnitude smaller. Finally, a high-frequency instability (3 to 10 times higher in frequency than the primary travelling instability) was measured near the breakdown of the stationary waves, and disappeared when the sensors were rotated ± 5 degrees. It is possible that this instability corresponds to the secondary instability of the stationary crossflow, but computations are needed for confirmation.

3. Based on a design from Prof. Zhong, the flared cone was fitted with strips of surface roughness in order to damp the second mode instability and delay transition. Pressure fluctuation measurements show that the roughness eliminated the second mode instability while amplifying the lower frequencies. TSP images show a delay in the onset of the second mode breakdown and transitional heating. It was also determined that the location of the initial roughness strip can control the extent of the damping and amplification of the instabilities. Lastly, roughness with increased spacing seems to damp the second mode while not amplifying lower frequencies. Further experiments are needed to explore this phenomenon.

4. Entropy-layer instability measurements have been made using surface pressure transducers and hot wires using a cone-ogive-cylinder with interchangeable nosetips. As the nosetip angle increases, the frequency of the instability decreases and the magnitude increases. The entropy-layer instability approaches the model with downstream distance[49] and the location varies smoothly with nosetip angle. Cross-correlations show that the surface and hot-wire sensors are measuring the same instability. They also indicate that it is a two-dimensional instability.

VII. Acknowledgements

This research is funded by the Air Force Office of Scientific Research under grant number FA9550-12-1-0167. Heath Johnson and Graham Candler at the University of Minnesota were very helpful in installing STABL on our Purdue computer and provided assistance in running the code.

References

[1]Chou, A., Ward, C. A. C., Letterman, L. E., Luersen, R. P. K., Borg, M. P., and Schneider, S. P., "Transition Research with Temperature-Sensitive Paints in the Boeing/AFOSR Mach-6 Quiet Tunnel," AIAA Paper 2011-3872, June 2011.

[2]Ward, C., Wheaton, B., Chou, A., Gilbert, P., Steen, L., and Schneider, S., "Boundary-Layer Transition Measurements in a Mach-6 Quiet Tunnel," AIAA Paper 2010-4721, June 2010.

[3]Luersen, R. P., *Techniques for Application of Roughness For Manipulation of Second-Mode Waves on a Flared Cone at Mach 6*, Master's thesis, School of Aeronautics and Astronautics, Purdue University, West Lafayette, IN, December 2012.

[4]Chynoweth, B., Ward, C., Henderson, R., Moraru, C., Greenwood, R., Abney, A., and Schneider, S., "Transition and Instability Measurements in a Mach 6 Hypersonic Quiet Wind Tunnel," AIAA Paper 2014-0074, January 2014.

[5]Sivasubrahmanian, J. and Fasel, H., "Direct Numerical Simulation of Controlled Transition In a Boundary Layer on a Sharp Cone at Mach 6," AIAA Paper 2013-0263, January 2013.

[6]Saric, W., Reed, H., and White, E., "Stability and Transition of Three-Dimensional Boundary Layers," *Annual Review of Fluid Mechanics*, Vol. 35, 2003, pp. 413–440.

[7]Deyhle, H. and Bippes, H., "Disturbance Growth in an Unstable Three-Dimensional Boundary Layer and its Dependence on Environmental Conditions," *Journal of Fluid Mechanics*, Vol. 316, December 1996, pp. 73–113.

[8]Saric, W. S., Jr., R. B. C., and Reibert, M. S., "Nonlinear Stability and Transition in 3-D Boundary Layers," *Meccanica*, Vol. 33, 1998, pp. 469–487.

[9]Corke, T., Matlis, E., Schuele, C.-Y., Wilkinson, S., Owens, L., and Balakumar, P., "Control of Stationary Cross-flow Modes Using Patterned Roughness at Mach 3.5," *7th IUTAM Symposium on Laminar-Turbulent Transition*, 2010, pp. 123–128.

[10]Schuele, C. Y., Corke, T. C., and Matlis, E., "Control of Stationary Crossflow Modes in a Mach 3.5 Boundary Layer Using Patterned Passive and Active Roughness," *Journal of Fluid Mechanics*, Vol. 718, 2013, pp. 5–38.

[11]Malik, M. R., Li, F., Choudhari, M. M., and Chang, C.-L., "Secondary Instability of Crossflow Vortices and Swept-Wing Boundary-Layer Transition," *Journal of Fluid Mechanics*, Vol. 399, 1999, pp. 85–115.

[12]Kohama, Y., "Some Expectations on the Mechanism of Cross-Flow Instability in a Swept-Wing Flow," *Acta Mechanica*, Vol. 66, February 1987, pp. 22–38.

[13]Poll, D. I. A., "Some Observations of the Transition Process on the Windward Face of Long Yawed Cylinder," *Journal of Fluid Mechanics*, Vol. 150, 1985, pp. 329–356.

[14]Choudhari, M., Li, F., Chang, C.-L., Carpenter, M., Streett, C., and Malik, M., "Towards Bridging the Gaps in Holistic Transition Prediction via Numerical Simulations," AIAA Paper 2013-2718, June 2013.

[15]Duan, L. and Choudhari, M. M., "Direct Numerical Simulation of Transition in a Swept-Wing Boundary Layer," AIAA Paper 2013-2617, June 2013.

[16]Schuele, C. Y., *Control of Stationary Cross-Flow Modes in a Mach 3.5 Boundary Layer Using Patterned Passive and Active Roughness*, Ph.D. thesis, University of Notre Dame, South Bend, Indiana, December 2011.

[17]Li, F., Choudhari, M., Chang, C.-L., and White, J., "Analysis of Instabilities in Non-Axisymmetric Hypersonic Boundary Layers over Cones," AIAA Paper 2010-4643, June 2010.

[18]Bendat, J. S. and Piersol, A. G., *Engineering Applications of Correlation and Spectral Analysis*, Wiley-Interscience, 2nd ed., 1980.

[19]Poggie, J., Kimmel, R. L., and Schwoerke, S. N., "Traveling Instability Waves in a Mach 8 Flow over an Elliptic Cone," *AIAA Journal*, Vol. 38, No. 2, February 2000, pp. 251–258.

[20]Borg, M. P., Kimmel, R., and Stanfield, S., "Traveling Crossflow Instability for HIFiRE-5 in a Quiet Hypersonic Wind Tunnel," AIAA Paper 2012-2821, June 2013.

[21]Kimmel, R. L., Demetriades, A., and Donaldson, J. C., "Space-Time Correlation Measurements in a Hypersonic Transitional Boundary Layer," *AIAA Journal*, Vol. 34, No. 12, December 1996, pp. 2484–2489.

[22]Malik, M. R., Li, F., and Chang, C. L., "Crossflow Disturbances in Three-Dimensional Boundary Layers: Nonlinear Development, Wave Interaction and Secondary Instability," *Journal of Fluid Mechanics*, Vol. 268, April 1994, pp. 1–36.

[23]Munoz, F., Heitmann, D., and Radespiel, R., "Instability Modes in Boundary Layers of an Inclined Cone at Mach 6," AIAA Paper 2012-2823, June 2012.

[24]Perez, E., Reed, H. L., and Kuehl, J. J., "Instabilities on a Hypersonic Yawed Straight Cone," AIAA Paper 2013-2879, June 2014.

[25]James, C., "Boundary-Layer Transition on Hollow cylinders in Supersonic Free Flight as Affected by Mach Number and a Screwthread Type of Surface Roughness," NASA Memo 1-20-59A, February 1959.

[26]Fujii, K., "Experiment of the Two-Dimensional Roughness Effect on Hypersonic Boundary-Layer Transition," *Journal of Spacecraft and Rockets*, Vol. 43, No. 4, July-August 2006.

[27]Wang, X. and Zhong, X., "Effect of wall perturbations on the receptivity of a hypersonic boundary layer," *Physics of Fluids*, Vol. 21, No. 4, 2009, pp. 044101–19.

[28]Fong, K. D., Wang, Z., and Zhong, X., "Numerical Simulation of Roughness Effect on the Stability of a Hypersonic Boundary Layer," *Computers and Fluids*, January 2014, pp. 1–18.

[29]Bountin, D., Chimitov, T., Maslov, A., Novikov, A., Egorov, I., Fedorov, A., and Utyuzhnikov, S., "Stabilization of Hypersonic Boundary Layer Using a Wavy Surface," *AIAA Journal*, Vol. 51, No. 5, May 2013.

[30]X. Zhong, K.D. Fong, X. W., "Roughness Design on a Proposed Roughness Experiments for the Purdue Compressible Cone for Mach-6 Quiet Tunnel," Private Communication - Email, January 2014.

[31]McKiernan, G. R. and Fisher, R. A., "Effects of 2-D Roughness Strips on a Flared Cone at Mach 6l," Final Report for Purdue AAE 520, June 2014.

[32]Schneider, S. P., "Paper 1 - Introduction and Goals," *NATO RTO-MP-AVT-200 - Hypersonic Laminar-Turbulent Transition*, San Diego, CA, April 2012.

[33]Reshotko, E., "Is Re_θ/M_e a Meaningful Transition Criterion?" *AIAA Journal*, Vol. 45, No. 7, 2007, pp. 1441–1443.

[34]Reshotko, E., *Hypersonic Flows for Reentry Problems*, chap. Hypersonic Stability and Transition, Springer-Verlag, Berlin, Germany, 1991.

[35]Stetson, K. F., "Comments on Hypersonic Boundary-Layer Transition," Tech. Rep. Final Report to AFRL Flight Dynamics Laboratory for the Period of October 1984 - July 1990 obtained from Steven P. Schneider, 1990.

[36]Anderson, J. D., *Modern Compressible Flow with Historical Perspective*, Vol. 1, The McGraw-Hill Companies, Inc., New York, New York, 3rd ed., 2003.

[37]Anderson, J. D., *Hypersonic and High-Temperature Gas Dynamics*, Vol. 1, American Institute of Aeronautics and Astronautics, Inc., Reston, Virginia, 1st ed., 1989.

[38]Lees, L. and Lin, C. C., "Investigation of the Stability of the Laminar Boundary Layer in a Compressible Fluid," Tech. Rep. Technical Note No. 1115, NACA, 1946.

[39]Reshotko, E., "Boundary Layer Instability, Transition and Control," *32nd Aerospace Sciences Meeting and Exhibit*, AIAA 94-0001, Reno, NV, January 1994.

[40]Dietz, G., Mahlmann, S., and Hein, S., "New Results in Numerical and Experimental Fluid Mechanics II," Chapter: Entropy-Layer Instabilities in Plane Supersonic Flow, Springer Fachmedien Wiesbaden, pp. 108-114, 1999.

[41]Stetson, K. F. and Rushton, G. H., "Shock Tunnel Investigation of Boundary-Layer Transition at M = 5.5," *AIAA Journal*, Vol. 5, No. 5, 1967, pp. 899–906.

[42]Stetson, K. F., "Nosetip Bluntness Effects on Cone Frustum Boundary Layer Transition in Hypersonic Flow," *16th Fluid and Plasma Dynamics Conference*, AIAA 83-1763, Danvers, MA, July 1983.

[43]Softley, E. J., Graber, B. C., and Zempel, R. E., "Experimental Observation of Transition of the Hypersonic Boundary Layer," *AIAA Journal*, Vol. 7, No. 2, 1969, pp. 257–263.

[44]Fedorov, A. V., "Instability of the Entropy Layer on a Blunt Plate in Supersonic Gas Flow," *Journal of Applied Mechanics and Technical Physics, Translated from Zhurnal Prikladnoi Mekhaniki i Tekhnicheskoi Fiziki*, Vol. 31, No. 5, 1990, pp. 722–728.

[45]Lysenko, V. I., "Influence of the Entropy Layer on the Stability of a Supersonic Shock Layer and Transition of the Laminar Boundary Layer to Turbulence," *Journal of Applied Mechanics and Technical Physics, Translated from Zhurnal Prikladnoi Mekhaniki i Tekhnicheskoi Fiziki*, Vol. 31, No. 6, 1990, pp. 868–873.

[46]Hein, S., "Nonlinear Nonlocal Transition Analysis," Tech. Rep. ISRN DLR-FB–2005-10, 2005.

[47]Stetson, K. F., Thompson, E. R., Donaldson, J. C., and Siler, L. G., "Laminar BoundaryLayer Stability Experiments on a Cone at Mach 8, Part 2: Blunt Cone," *22nd AIAA Aerospace Sciences Meeting and Exhibit*, AIAA 84-0006, Reno, NV, January 1984.

[48]Ward, C. A. C., Greenwood, R. T., Abney, A. D., and Schneider, S. P., "Boundary-Layer Transition Experiments in a Hypersonic Quiet Wind Tunnel," *AIAA 43rd Fluid Dynamics Conference*, AIAA 2013-2738, San Diego, CA, June 2013.

[49]Chynoweth, B. C., Ward, C. A. C., Henderson, R. O., Moraru, C. G., Greenwood, R. T., Abney, A. D., and Schneider, S. P., "Transition and Instability Measurements in a Mach 6 Hypersonic Quiet Wind Tunnel," *52nd AIAA Aerospace Sciences Meeting*, AIAA 2014-0074, National Harbor, MD, January 2014.

[50]Greenwood, R. T., *Experimental Measurement of Entropy-Layer Instabilities over a Cone-Ogive-Cylinder at Mach 6 (estimated publication date: July 2014)*, Ph.D. thesis, School of Aeronautics and Astronautics, Purdue University, West Lafayette, IN, 2014.

[51]Johnson, H. B. and Candler, G. V., "Hypersonic Boundary Layer Stability Analysis Using PSE-Chem," *35th Fluid Dynamics Conference*, AIAA 2005-5023, Toronto, Canada, June 2005.

[52]Rufer, S. J., *Hot-Wire Measurements of Instability Waves on Sharp and Blunt Cones at Mach 6*, Ph.D. thesis, Department of Aeronautics and Astronautics, Purdue University, West Lafayette, IN, 2005.